Improved empirical force field for multicomponent oxide glasses and crystals

Marco Bertani ⓘ, Maria Cristina Menziani ⓘ, and Alfonso Pedone ⓘ*

Department of Chemical and Geological Sciences, University of Modena and Reggio Emilia, via G. Campi 103, 41125 Modena, Italy

In this paper, the self-consistent PMMCS force fields (FFs) [Pedone *et al.*, J. Phys. Chem. B **110**, 11780 (2006)] widely used for the simulation of a large variety of silicates, aluminosilicate and phosphate crystals, and multicomponent oxide glasses have been revised and improved by the inclusion of two types of three-body interactions acting between T-O-T bridges (T = Si and P) and network former-network former repulsive interactions. The FFs named Bertani–Menziani–Pedone (BMP)-harm and BMP-shrm better reproduce the T-O-T bond angle distributions (BADs) and network former-oxygen distances. Consequently, the prediction of Q^n distributions (Q stands for quaternary species, and n is the number of bridging oxygens around it), neutron total distribution functions, solid-state nuclear magnetic resonance spectra of spin active nuclei (^{29}Si, ^{17}O, ^{31}P, ^{27}Al), and the density have also been hugely improved with respect to the previous version of our FF. These results also highlight the strong correlation between the T-O-T BADs and the other short and intermediate structural properties in oxide glasses, which have been largely neglected in the past. In addition to the improvement of the structure, the FF has been revealed to reproduce well the ionic conductivity in mixed alkali aluminosilicate glasses and the elastic properties. The systematic comparison with other interatomic potential models, including the polarizable core-shell model, carried out in this paper showed that our potential model is more balanced and effective for simulating a vast family of crystalline and amorphous oxide-based systems.

I. INTRODUCTION

Multicomponent oxide glasses play a key role in addressing major global challenges in energy, medicine, and advanced communications systems [1,2] and are thus among the more used materials in the related industries.

Being disordered materials, glasses do not have to fulfill stoichiometric restraints as crystals do, and thus, their chemical composition is largely tunable, leading to a vast number of structures with uniquely refined combinations of properties [3]. Unfortunately, the development of glass compositions with tailored properties is hampered by the lack of a complete understanding of the structure of multicomponent oxide glasses. This is understood as a continuous random network of coordination polyhedra made of the network-forming cations (T = Si, P, B, Ge) and oxygen. Cation-oxygen polyhedra like SiO_4 in vitreous silica, PO_4 in phosphate glasses, or BO_3 in vitreous boron oxide are usually corner linked through bridging oxygens (BOs). Whereas, in v-SiO_2 and v-B_2O_3, all oxygen ions surrounding Si and B are bridging among two polyhedral, in v-P_2O_5, each polyhedron is connected to three others because of the formation of a terminal double P = O bond [3].

Structural disorder in a glass network leads to statistical distribution of angles and unconstrained dihedral angles between the polyhedra. The addition of network-modifying alkali and/or alkaline-earth ions in silicates and phosphate glasses breaks up the connectivity of the oxide network with

the creation of terminal anions, called non-BOs (NBOs), which are linked to only one network-forming cation [4,5].

When Al_2O_3 is introduced into a modified silicate glass composition, Al cations predominantly form negatively charged $(AlO_4)^{1-}$ units that are charge compensated by the modifying cations, and the concentration of NBO is reduced accordingly. It becomes nominally zero when the ratio Al/Na = 1 [6]. Instead, if no modifier cations are available, Al can create NBO and forms higher coordination states (as AlO_5 and AlO_6) strongly affecting several important properties.

The complexity of the glass structure hugely increases in multicomponent oxide glasses where more network formers and modifiers are mixed.

Molecular dynamics (MD) simulations based on empirical interatomic potentials have emerged as a powerful and efficient tool to gain insights into the composition-structure-properties relationships of a wide range of amorphous and glassy materials [7–9] and are being more often used to train machine learning algorithms [10,11]. However, the accuracy and reliability of classical MD results strongly depend on the interaction potential used, and thus, great efforts have been devoted over decades for developing accurate potentials for oxide glasses [12–17].

Most interatomic potentials developed were based upon the rigid ionic model (RIM) and only a few on models including polarizability effects such as the core-shell model (CSM) proposed by Dick and Overhauser [18] and the polarizable ion model (PIM) developed by Aguado *et al.* [19]. In the RIM, all ions are treated as fixed-point charges; in the CSM, the anions are represented by a positive massive core connected

---

*Corresponding author: alfonso.pedone@unimore.it

to a negative massless shell through a harmonic spring; and in the PIM, a dipole polarizability and an induced dipole moment (determined minimizing the polarization energy term) are associated to each ion.

Among the force fields (FFs) based on the RIM, we mention the pairwise interatomic potentials proposed by Teter [20] and largely employed and modified by Du's group [8], the one proposed by us and known as Pedone's or PMMCS potentials [7,12], and the one more recently developed in the group of Sundararaman et al. [13] and known as the SHIK potentials.

PMMCS potentials make use of the Morse function for short-range interactions whose parameters were fitted to structural and elastic properties of various oxide and silicate crystals. The availability of parameters for many cation-oxygen pairs and its ability to predict the mechanical properties fairly accurately have made it a very popular choice for the study not only of multicomponent oxide glasses but also crystalline materials and oxide nanoparticles [21–29].

Although the interatomic potentials reproduce the short-range structure of silicate glasses well, they share the same deficiency, that is, large discrepancies in the Q^n distributions of network former species [30]. Shell model MD simulations have been revealed to better reproduce the Q^n distributions for Si and P cations in soda-lime silicates, aluminosilicate, phosphosilicate, and phosphate glasses [15,31–36] and vibrational properties [37]. Moreover, we showed that the structural models of silicate, aluminosilicate, and borosilicate glasses generated using the CSM provide computed nuclear magnetic resonance (NMR) spectra in better agreement with experiments because this model better reproduces the T-O-T ($T =$ Si, P, Al, B) bond angle distributions (BADs) than the RIM [38,39]. In a recent investigation, we also showed that the CSM accurately reproduces the ionic conductivity trends in mixed alkali aluminosilicate glasses [40].

The questions that naturally arose from these previous investigations were: (i) How important is the Si-O-Si BAD, which has been often undervalued in previous papers, to reproduce glass structure and properties? (ii) Does the CSM better reproduce the medium-range structure, the NMR spectra, and other important properties because of its ability to provide narrower Si-O-Si angles or because of the inclusion of polarizability?

To respond to these queries, we have revised the original PMMCS FFs by including T-O-T ($T =$ Si and P) three-body interactions and T-T network former repulsive interactions and benchmarked its performance as well as the original PMMCS, SHIK, and CSM FFs in reproducing the structure and several other properties of silicate, aluminosilicate, phosphate, and phosphosilicate glasses against experimental data.

II. COMPUTATIONAL DETAILS

A. FF description

Five interatomic potential models were examined: the pairwise RIMs proposed by Pedone et al. [7,12], and Sundararaman et al. [13], named PMMCS and SHIK potentials hereafter, two modified PMMCS potentials with the inclusion of two different kinds T-O-T three-body interactions developed in this paper (BMP-harm and BMP-shrm), and the CSM with Si-O, Al-O, P-O, Na-O, K-O, and O-O parameters taken

from Refs. [15,41,42]. Moreover, a parameter set for the Li ion of the CSM has also been developed here since it was absent in the literature. The functional forms and parameters of the PMMCS and BMP potentials are described in the following, whereas those of the SHIK and CSM are reported in Tables SI and SII of the Supplemental Material [43].

1. PMMCS potentials

The original version of the PMMCS potential combines a long-range Coulomb potential and a short-range Morse function with a repulsive contribution of the form B_{ij}/r^{12} to prevent atomic collapse at high temperature and pressure:

$$U_{ij}(r_{ij}) = \frac{z_i z_j e^2}{r_{ij}} + D_{ij}\left(\left\{1 - \exp\left[-a_{ij}\left(r_{ij} - r_{ij}^0\right)\right]\right\}^2 - 1\right) + \frac{B_{ij}}{r_{ij}{}^{12}}, \tag{1}$$

where D_{ij}, a_{ij}, and r_{ij}^0 are the parameters for the i-j pairs of the Morse function, B_{ij} is the parameter of a repulsive term acting at short distances to prevent collapse of atoms at high temperature, and z_i are the partial charges of ions i, which are described as rigid cores; the partial charges on the cations are referred to as the fixed charge of $-1.2e$ assigned to the oxygen. The PMMCS potential was parameterized to reproduce the experimental crystal structures and properties such as elastic constants of oxides, silicates, and aluminosilicates. The parameter set is reported in the original Refs. [7,12,35,40].

2. BMP potentials

The BMP potentials originate from the PMMCS with the inclusion of network former-network former repulsive Buckingham potentials ($A_{ij}e^{-r_{ij}/\rho_{ij}}$) and three-body interactions. Two versions of this potential differing by the three-body functional form used have been developed. In the first version, called BMP-harm a simple harmonic functional form has been used:

$$U(\theta_{ijk}) = \frac{k_{ijk}}{2}(\theta_{ijk} - \theta_{ijk,0})^2, \tag{2}$$

whereas, in the second version, named BMP-shrm, the following screened harmonic functional form has been used:

$$U(\theta_{ijk}) = \frac{k_{ijk}}{2}(\theta_{ijk} - \theta_{ijk,0})^2 \exp\left[-\left(\frac{r_{ij}}{\rho} + \frac{r_{jk}}{\rho}\right)\right]. \tag{3}$$

In both cases, k_{ijk} and $\theta_{ijk,0}$ are parameters connected to the force constant and reference angle of the i-j-k triplet. The Si-O-Si, P-O-P, and Si-O-P triplets have been included.

The rationale and physical bases behind the inclusion of these terms is that the T-O-T equilibrium angle in partially covalent systems like the ones investigated here are the results of the balance between the Coulombic repulsion of the TO$_4$ tetrahedra and the two lone pairs on the BO, which in valence bond theory [44] is represented by sp^3 hybridization. This has also been demonstrated by post-Hartree–Fock calculations on pyrosilisic acid molecules [45]. The $\theta_{ijk,0}$ parameters of the triplets of interest have thus been kept fixed at 109.47° (which is the reference angle for hybrid sp^3 orbitals). Obviously, this

is a simplified view of the complex interplay between different classical and quantum effects governing the electronic structure of these systems and their geometry. We emphasize that other choices of the reference angle could be done, for example, by treating it as fitting parameters or using some experimental value, but the physical meanings could be questionable since the Si-O-Si angle does not have a unique value in silicates. The same is true for the other triplets included.

To reduce the number of parameters to optimize, the ρ parameter in the shrm functional form has also been fixed to 1.0 Å (a value used in the CSM O-T-O three-body terms in previous papers [15]). The force constants k_{ijk} and the A_{ij} and ρ_{ij} parameters for the Si-Si, Si-Al, Si-P, P-P, Al-Al, and Al-P pairs have been fitted on the structure of several crystalline structures (α-quartz, Na_2SiO_3, $Na_2Si_2O_5$, $Na_6Si_8O_{19}$, $Na_2Si_3O_7$, Li_2SiO_3, $Li_2Si_2O_5$, $K_2Si_2O_5$, $K_2Si_4O_9$, $K_6Si_4O_9$, $Na_{31}K_9Si_{40}O_{100}$, $KLiSiO_5$, $NaAlSi_2O_6$, $NaAlSiO_4$, $KAlSiO_4$, $KAlSi_2O_6$, $KAlSi_3O_8$, $LiAlSi_2O_6$, P_2O_5 (*Fmmm* space group), P_4O_{10} (*R-3m*), $Ca_2P_2O_7$, and $Na_4P_2O_7$) using the relaxed-fitting method implemented in GULP [46]. It is worth highlighting that BMP-harm and BMP-shrm share all FF parameters with the exception of the force constant in the three-body functions.

In any fitting procedure, the aim is to minimize the sum of squares function F defined as follows:

$$F = \sum_{i=1}^{M} w_i (f_{i,\text{obs}} - f_{i,\text{MM}})^2, \quad (4)$$

where M is the total number of observables used during fitting, w_i is a weighting factor for each observable, and $f_{i,\text{obs}}$ and $f_{i,\text{MM}}$ are the experimental or QM-computed (Qantum Mechanical) and the MM-computed (Molecular Mechanic) observables, respectively.

In the relaxed-fitting method, $f_{i,\text{MM}}$ are the observables (structure and properties) computed after a geometry optimization. This means that the structure is optimized at every step in the fit, and the displacements of the structural parameters are calculated instead of the energy gradients as used in conventional fitting. In this paper, apart from the structure of the crystalline phases, we explicitly included as observables the angles of the triplets. It is worth highlighting that the force constants have been fitted first to better reproduce the T-O-T angles, whereas the cation-cation repulsive interactions have been subsequently fitted to better reproduce the T-T distances and the volume of the unit cell of the crystals.

It is also important to highlight that, during the fitting of the original Li-O and K-O Morse parameters in the PMMCS potentials, the elastic constants were not included since the experimental values of the $Li_2Si_2O_5$ and $K_2Si_2O_5$ crystals were not available. In this paper, we have refined these parameters by fitting on the Young's and bulk moduli computed at the density functional theory (DFT) Perdew–Burke–Ernzerhof (PBE) functional revised for solids [47] level using the CASTEP code [48]. During the P-O-P three-body interaction fitting, the r_0 parameter of the P-O Morse function was modified, decreasing it by 0.01 Å to better reproduce the P-O bond distance. The parameters of the pairwise and three-body in-

TABLE I. The parameters for the pair interactions used in this paper for the BMP-harm and BMP-shrm potentials. The Li-O, K-O, and P-O parameters have been modified with respect to the original PMMCS potential, whereas the Si-Si, Si-Al, Si-P, Al-Al, and P-P repulsive interactions have been added since they were not considered in the original PMMCS potential [7,12].

Morse parameters				
Atom pairs	D_{ij} (eV)	a_{ij} (Å^{-2})	r_0 (Å)	B_{ij} (eVÅ^{12})
$Si^{2.4}$-$O^{-1.2}$	0.340554	2.006700	2.100000	1.0
$Al^{1.8}$-$O^{-1.2}$	0.361581	1.900442	2.164818	0.9
$P^{3.0}$-$O^{-1.2}$	0.831326	2.585833	1.790790	1.0
$Na^{0.6}$-$O^{-1.2}$	0.023363	1.763867	3.006315	5.0
$K^{0.6}$-$O^{-1.2}$	0.016098	2.067900	3.180030	5.0
$Li^{0.6}$-$O^{-1.2}$	0.041556	1.758181	2.551360	1.0
$Ca^{1.2}$-$O^{-1.2}$	0.030211	2.241334	2.923245	5.0
$O^{-1.2}$-$O^{-1.2}$	0.042395	1.379316	3.618701	100.0

Buckingham parameters		
Atom pairs	A_{ij} (eV)	ρ_{ij} (Å^{-2})
Si-Si	7.093669	0.975598
Si-Al	8.090830	0.521919
Si-P	5.093669	0.905598
Al-Al	7.059690	0.919844
P-P	5.093669	0.905598

Harmonic three-body potential parameters (BMP-harm)		
Triplets	k_b (eV rad^{-2})	θ_0 (deg)
Si-O-Si	0.73	109.47
P-O-P	2.00	109.47
Si-O-P	2.00	109.47

Screened harmonic three-body potential parameters (BMP-shrm)			
Triplets	k_b (eV rad^{-2})	θ_0 (deg)	ρ (Å)
Si-O-Si	25.0	109.47	1.0
P-O-P	65.0	109.47	1.0
Si-O-P	120.0	109.47	1.0

teractions of the BMP potential used in this paper are reported in Table I.

The original pairwise interaction parameters of the PMMCS potential are reported in Refs. [7,12,49]. We stress the fact that the BMP potentials use the same pairwise parameters of the PMMCS except for the Li-O, K-O, and P-O ones which have been slightly modified, as stated above.

The plots of the experimental vs calculated T-O-T angles and densities of the crystals used in the fitting procedure are reported in Fig. 1.

The figure shows that the BMP parameterizations reproduce much better the T-O-T angles, especially the P-O-P and Si-O-Si ones, the angles for which the three-body interactions have been included. In fact, the P-O-P angles are reproduced with an average error of 21.1°, 8.7°, and only 3.4° for PMMCS, BMP-shrm, and BMP-harm potentials, respectively. The average error on the Si-O-Si angles reduces from 5.2° for PMMCS to 2.8° with the BMP-harm and 2.7° with the BMP-shrm potential. The Si-O-Al angles, which are free of three-body interactions, present an average error of 2.9°, 2.8°, and 2.5° for PMMCS, BMP-shrm, and BMP-harm, respectively. The average error on the Al-O-Al angles, which is also free of three-body interaction, decreases from 4.6°
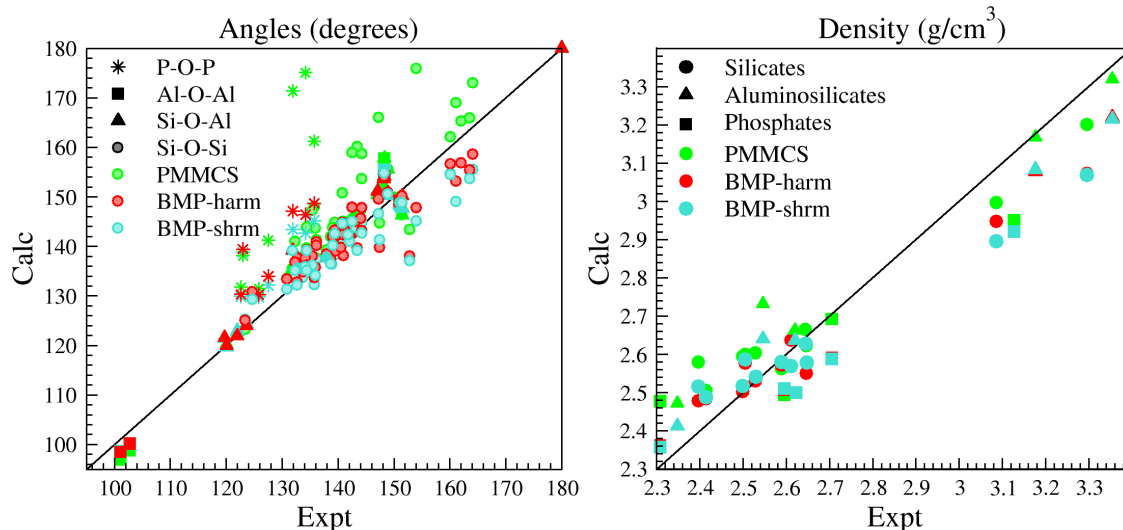
FIG. 1. Experimental vs calculated T-O-T angles (left) and density (right) of the crystal phases used in fitting procedure obtained using the PMMCS (green symbols), BMP-shrm (cyan symbols), and BMP-harm (red symbols) potentials. Linear regression has been made on data of each potential, giving the following linear equations and correlation coefficient (R^2) for the angles: $Y_{PMMCS}(x) = 0.969x + 10.308$, $R^2 = 0.718$; $Y_{BMP\text{-}shrm}(x) = 0.866x + 19.608$, $R^2 = 0.870$; $Y_{BMP\text{-}harm}(x) = 0.905x + 14.130$, $R^2 = 0.909$. The same procedure has been applied to the density data, giving the following equations and correlation coefficients (R^2): $Y_{PMMCS}(x) = 0.812x + 0.527$, $R^2 = 0.883$; $Y_{BMP\text{-}shrm}(x) = 0.759x + 0.603$, $R^2 = 0.897$; $Y_{BMP\text{-}harm}(x) = 0.795x + 0.513$, $R^2 = 0.914$.

for PMMCS to 3.5° with BMP-shrm and 3.2° with BMP-harm. Therefore, the introduction of three-body terms for the Si-O-Si and P-O-P triplets also improves the value of the angle of the triplets involving Al ions. It is worth highlighting that, in general, the larger errors found with the BMP potentials are found for angles above 150°. To improve the reproduction of these broad angles, a different three-body functional form dependent on an exponential decaying term with the angle of the type $\exp[-(\theta - \theta_0)/\rho]$ should be used. Linear regression has been applied to the data obtained with different potentials (the equation of the lines and correlation coefficients can be found in the legend of Fig. 1). It is noteworthy that PMMCS provides the best slope of the regression straight line (0.97), so the closest to one, but it shows the worst correlation coefficient ($R^2 = 0.72$), which indicates a large dispersion of the data. BMP-shrm and BMP-harm provide lower slopes of 0.87 and 0.91, respectively, because of their difficulties in the prediction of large angles, but they show higher R^2 of 0.87 and 0.91, respectively, that reflect a minor dispersion of data. The right panel of Fig. 1 shows that the density of the crystals is reproduced with similar accuracy by the PMMCS and both the BMP potentials. The average errors are 3.6%, 3.4%, and 2.9% for PMMCS, BMP-shrm, and BMP-harm, respectively. Even in this case, a linear regression of the three series of data obtained with the different potentials has been performed (the equation of the straight lines and correlation coefficient can be found in the caption of Fig. 1), leading to the same considerations made for the angles.

B. Generation of glass structure and properties calculations

Glass structural models containing about 1500 atoms were generated through the melt and quench approach by MD simulations except for the binary alkali-silicate glass models used to compute the Young modulus with the dynamic method

(data reported in sec. 2.2.2 of the Supplemental Material [43]) for which boxes containing about 10 000 atoms were used. [7] Four replicas of each glass model have been examined to confirm the reproducibility of the results and to estimate the variability in the glass properties. A detailed description of the computational procedure is reported in the Supplemental Material [43]. The structural models were then analyzed to determine their structural features (bond distances, coordination numbers, BADs, Q^n distributions, ring size distributions), the neutron total distribution functions (TDFs), elastic properties, and ionic conductivities are also described in the Supplemental Material [43]. As for the NMR calculations, we used glass models containing about 400 atoms, computed the NMR parameters (shielding and electric field gradients) at the DFT-PBE level using the NMR-CASTEP code [48] and using the SoSNMR [50] code to simulate the Magic Angle Spinning (MAS) spectra spectra of ^{29}Si, ^{17}O, ^{27}Al, and ^{31}P elements. All details are reported in the Supplemental Material [43]. It is important to highlight that, before the NMR calculations, the structural models were relaxed at the molecular mechanics level with the five interatomic potentials used to generate them. This procedure differs from the usual MD gauge-including projector augmented wave approach used in our previous papers [38,39,51], where the structural models are relaxed at the DFT level, but it allows better comparison of the performance of the interatomic potentials models.

III. THE GLASS COMPOSITIONS

Table II lists the set of 40 modeled glasses used to validate the BMP FFs. The glasses belong to several important families: pure silica, alkali silicates, single and mixed alkaline aluminosilicates, calcium-sodium phosphates, and phospho-silicate glasses. Vitreous P_2O_5 has not been simulated because

TABLE II. Compositions and density of the glasses investigated.

Glass family	Glass name	Composition							Density (g/cm^3)
		%K$_2$O	%Li$_2$O	%Na$_2$O	%CaO	%Al$_2$O$_3$	%SiO$_2$	%P$_2$O$_5$	
Silicates	SiO$_2$						100.0		2.200
	LS10		10.0				90.0		2.235
	LS15		15.0				85.0		2.254
	LS20		20.0				80.0		2.283
	LS25		25.0				75.0		2.301
	LS30		30.0				70.0		2.33
	LS33		33.0				67.0		2.349
	LS40		40.0				60.0		2.346
	NS10			10.0			90.0		2.289
	NS15			15.0			85.0		2.328
	NS20			20.0			80.0		2.383
	NS25			25.0			75.0		2.418
	NS30			30.0			70.0		2.466
	NS33			33.0			67.0		2.496
	NS40			40.0			60.0		2.532
	NS50			50.0			50.0		2.56
	KS10	10.0					90.0		2.305
	KS15	15.0					85.0		2.341
	KS20	20.0					80.0		2.389
	KS25	25.0					75.0		2.417
	KS30	30.0					70.0		2.453
	KS33	33.0					67.0		2.472
	KS40	40.0					60.0		2.489
Aluminosilicates	NAS*R*-0.7			29.4		29.4	41.2		2.502
	NAS*R*-1			25.0		25.0	50.0		2.498
	NAS*R*-3			12.5		12.5	75.0		2.38
	NAS*T*-1.5			15.8		23.0	61.2		2.4711
	NAS*T*-1			18.1		18.1	63.8		2.4702
	NAS*T*-0.6			22.8		15.6	61.6		2.4478
	SAN			25.0		10.0	65.0		2.455
	SANK	12.5		12.5		10.0	65.0		2.465
	SAK	25.0		0.0		10.0	65.0		2.477
Phosphates	NP			50.0				50.0	2.47
	NCP			10.0	40.0			50.0	2.61
	CP				50.0			50.0	2.59
Phosphosilicates	NCPS_2.11			24.6	26.7		46.1	2.6	2.704
	NCPS_2.30			24.2	26.4		45.4	4.0	2.704
	NCPS_2.54			24.1	23.3		48.6	4.0	2.65
	NCPS_2.74			20.2	22.2		55.0	2.6	2.64
	NCPS_2.93			17.9	23.3		54.8	4.0	2.639

its high hygroscopicity makes it difficult to find experimental data to compare with the results obtained by our dry models.

The glasses are labeled by acronyms created using the capital letters of the glass network modifiers (Na, Li, K, and Ca), intermediate (Al), or former (Si and P) cations. In the case of the binary alkali silicate glasses, the final number represents the molar percentage of the modifier oxide in the composition, that is, LS20 refers to $20Li_2O \cdot 80SiO_2$ composition. The structure and properties of binary alkaline silicate glasses as a function of alkali content have been deeply investigated in the past and thus provided us many accurate data values to compare with: densities, neutron TDFs, coordination number and bond distances, Q^n distributions, ^{29}Si and ^{17}O MAS NMR spectra, and elastic constants.

Three different series have been chosen for aluminosilicates glasses: the series NAS*R*-x is composed of charged-balanced aluminosilicates with varying Si/Al ratios ($R = 0.7$, 1.0, and 3), the series NAS*T*-x is composed of sodium aluminosilicates with varying Al/Na ratios ($T = 0.6$, 1.0, and 1.5). In the last series (SAN, SANK, and SAK glasses), the amount of Si and Al ions are kept constant, whereas sodium is replaced by potassium ions. For these glasses, information on the density, coordination numbers, and distances, ^{29}Si, ^{17}O, and ^{27}Al MAS NMR spectra, the population of Si-O-Si, Si-O-Al, and Al-O-Al bonds, as well as elastic constants and ionic conductivity is available [6,52]. The last two series investigated belonging to the phosphate (NCP) and phosphosilicate (NCPS) families are of great interest for biomedical research
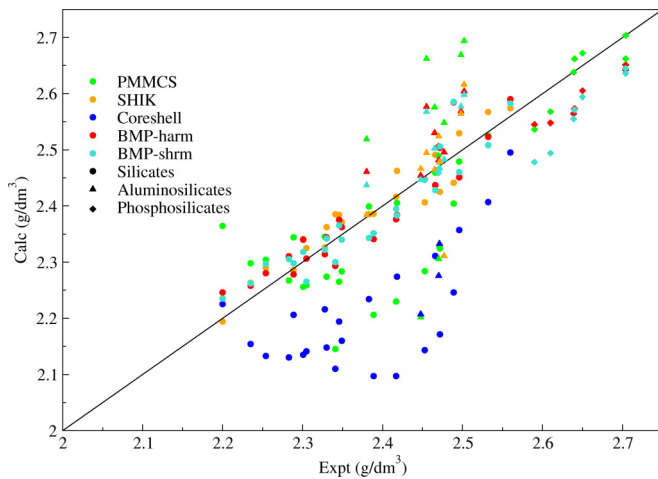
FIG. 2. Correlation plot between the experimental and calculated densities of the glasses investigated using the different potentials. Linear regression has been made on data obtained with each potential, giving the following straight line equations and correlation coefficients (R^2): $Y_{PMMCS}(x) = 0.988x + 0.015$, $R^2 = 0.569$; $Y_{SHIK}(x) = 0.964x + 0.099$, $R^2 = 0.795$; $Y_{Coreshell}(x) = 0.684x + 0.584$, $R^2 = 0.433$; $Y_{BMP\text{-}harm}(x) = 0.857x + 0.353$, $R^2 = 0.848$; $Y_{BMP\text{-}shrm}(x) = 0.820x + 0.435$, $R^2 = 0.830$.

and include CaO, which has a huge effect on their structures and properties. The NCPS phosphosilicate glasses are labeled by their silicate network connectivity (average number of BOs per silicon), owing to its direct relevance for bioactivity [53]. Densities, neutron TDFs, bond distances, phosphorous Q^n distribution functions, and ^{31}P NMR spectra are available [54].

IV. RESULTS AND DISCUSSIONS

A. Density

Density is one of the first and easily measured properties of glasses, and its knowledge has often been exploited to fix the system volume in the computational investigation of glass structure. It is for this reason that the performances of FFs in the reproduction of the density of oxide glasses were often overlooked in the past. However, with the increasing use of MD simulations to predict properties of multicomponent glasses not yet synthesized, the need of FFs able to reproduce the density accurately has become mandatory to computational glass scientists.

A correlation plot between the densities computed using the PMMCS, SHIK, CSM, BMP-shrm, and BMP-harm potentials against the experimental ones is reported in Fig. 2. The PMMCS significantly underestimates the density of alkali silicates and overestimates that of v-silica and aluminosilicates, whereas the BMP and SHIK potentials predict them quite well. CSM always underestimates the density of the studied glasses. By considering only the silicates and aluminosilicate glasses, the mean absolute error (MAE) of PMMCS, CSM, SHIK, BMP-shrm, and BMP-harm potentials are 0.099, 0.172, 0.033, 0.033, and 0.037 g/cm³, respectively.

CSM potentials reproduce badly both the silicate and aluminosilicate glasses with MAEs of 0.176 and 0.191 g/cm³.

For this reason, we decided not to compute the density for phosphate and some of the aluminosilicate glasses but only the structure and other properties using the moles, volume, and temperature ensemble to quicken the investigation. This decision has been taken after checking that all properties (as Q^n distribution, bond distances, and BAD) of the glasses already simulated in the particles, pressure, and temperature ensemble do not change significantly by changing the ensemble. The PMMCS potentials reproduce better the density of the phosphate/phosphosilicate (MAE = 0.021 g/cm³) and binary silicate/v-silica glasses (MAE = 0.075 g/cm³) than the aluminosilicates (MAE = 0.16 g/cm³). The MAEs for binary silicates/v-silica are 0.026, 0.029, and 0.030 g/cm³ for SHIK, BMP-shrm, and BMP-harm potentials and 0.052, 0.044, and 0.054 g/cm³ for aluminosilicates. BMP-shrm and BMP-harm give MAEs of 0.072 and 0.056, respectively, for phosphate and phosphosilicate glasses. Instead, the SHIK potential does not contain parameters for phosphorous.

The equations of the regression straight lines with their relative correlation coefficients for all studied potentials are reported in the caption of Fig. 2. They show that BMP-shrm and BMP-harm provide lower slopes (0.82 and 0.86, respectively) with respect to SHIK (0.96) and PMMCS (0.94), but higher correlation constants ($R^2 = 0.83$ and 0.85 for BMP-shrm and BMP-harm and 0.80 and 0.52 for SHIK and PMMCS). CSM provides the worst R^2 value (0.43) with the lower slope (0.61).

Figure S2 of the Supplemental Material [43] reports the trends of the experimental and computed density values as a function of the compositions of the different series. CSM potentials never correctly reproduce the experimental density trends. In fact, they present an unphysical minimum in both the LS and KS series. The PMMCS potential provides good results only for the phosphate series and for the binary silicate containing sodium, while it shows the opposite trend for the LS and a minimum in the KS series. Moreover, it gives poor results in all aluminosilicate series. Instead, SHIK and the two BMPs potentials reproduce the trends of all silicate and aluminosilicate series investigated except for the NAS*T* series. The SAN/K densities are extremely well reproduced by BMP-shrm. The BMP-harm potential provides good trends also for the phosphate/phosphosilicate series, while BMP-shrm slightly underestimates the density of the NCP glasses.

B. Neutron TDFs

Figure 3 reports the comparison between the simulated neutron TDF with different FFs and the experimental one for the binary alkali silicate LS33, NS30, and KS33 and for the sodium and calcium phosphate glasses NP, CP, and NCP, whereas Fig. S3 of the Supplemental Material [43] that of silica glass.

All interatomic potentials reproduce well the positions of the first two peaks at around 1.6 and 2.6 Å that arise from the Si-O and O-O pair distances in silicate glasses. Major differences are observed in the shapes, the peak intensities, and on the peaks associated with the medium-range order defined by the cation-cation pair distribution distances above 3.0 Å.

To quantify the agreement between the computed total correlation function $T^{sim}(r)$ with the diffraction data $T^{exp}(r)$,
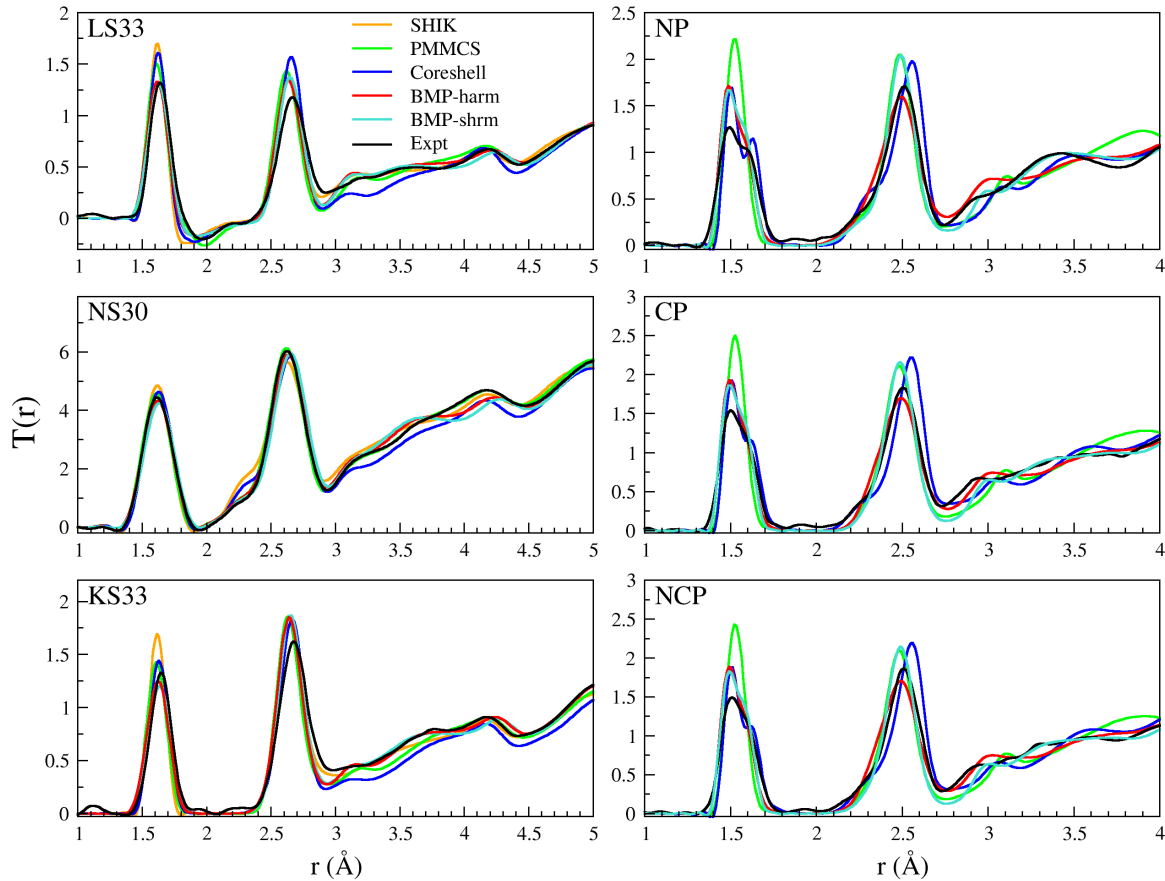
FIG. 3. Simulated and experimental total neutron distribution functions of the binary alkali silicate LS33, NS30, and KS33 glasses and sodium, calcium phosphate NP, NCP, and CP glasses.

the former has been broadened to account for the limit of the momentum transfer (Q_{max}) in diffraction experiments (see Supplemental Material [43]) [55], and then the R_x factor proposed by Wright has been computed [56]

$$R_x = \left\{ \frac{\sum_{i=1}^{N} [T^{exp}(r_i) - T^{sim}(r_i)]^2}{\sum_{i=1}^{N} [T^{exp}(r_i)]^2} \right\} 100, \qquad (5)$$

It is interesting to note that, apart from the NS33 glass, the two BMP potentials present the smallest R_x factor: 12.7 and 12.0 for LS33 and KS33 with BMP-harm and 9.7 for both the glasses with BMP-shrm. The PMMCS FF provides the smallest R_x factor (2.7) for the NS33 glass, but the values obtained with BMP FFs (3.8 and 6.8 with BMP-harm and BMP-shrm, respectively) are smaller than those provided by the SHIK (6.9) and CSM (7.8) potentials. PMMCS, SHIK, and CSM potentials provide higher R_x values for KS33 and LS33: 17.2 and 18.9 with PMMCS, 15.4 and 17.4 with SHIK, and 17.4 and 18.7 with the CSM.

Overall, it seems that the structure of binary alkali silicate glasses obtained with the two BMP potentials is in better agreement with experiments with respect to the one obtained with the PMMCS, SHIK, and CSM potentials and that the BMP-harm better reproduces the structure of NS30, while lithium and potassium silicate structures are better reproduced with BMP-shrm.

As for the phosphate glasses, the two BMPs better reproduce the position of the first peak of the spectra around 1.5, relative to the P-O pair distance. The position of the second peak is underestimated by the PMMCS and BMP-shrm potentials and overestimated by the CSM, while BMP-harm gives a very good overlapping with the experimental peak. The intensity of the first peak is overestimated by all FFs, especially by the PMMCS. It is noteworthy that, in the experimental distribution, the first peak shows a shoulder around 1.6 Å for all three studied glasses due to the different distances of P-NBO and P-BO bonds around 1.5 and 1.6 Å, respectively. PMMCS potential does not reproduce this shoulder, while it is present in both the BMP and CSM spectra. The latter overestimates the position of the P-BO peak, generating a double peak, while the two BMPs show the best agreement with experimental data. The R_x values for these glasses confirm the superiority of the BMP data over the ones obtained with the other tested potentials, showing values of 12.6, 10.2, and 11.2 for NP, CP, and NCP, respectively, with BMP-harm and 13.8, 12.8 and 13.1 with BMP-shrm, while the CSM provides 16.7, 16.8, and 15.8 and PMMCS 23.8, 20.9, and 20.8.

C. Bond distances

The Si-NBO, Si-BO, M-O (M = Li, Na, and K), and Al-O pair distribution functions (PDF) of the LS33, NS33, and KS33 glasses as representative of the binary alkali silicate
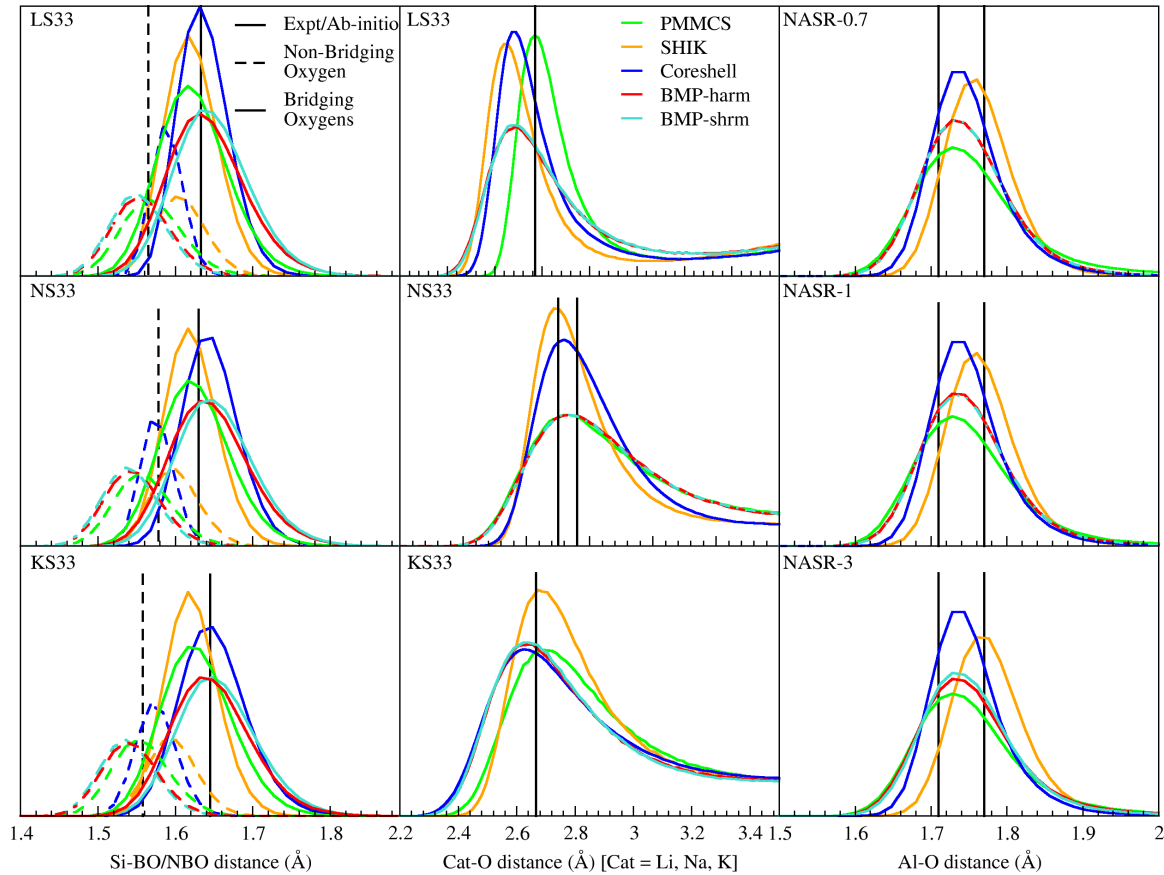
FIG. 4. Si-O, M-O (M = Li, Na, and K), and Al-O pair distribution functions of the LS33, NS33, and KS33 glasses and of the NASR series for the aluminosilicate glasses.

glasses and of the NASR series for the aluminosilicate glasses are shown in Fig. 4. Experimental or *ab initio* distances are reported as black vertical lines in the figure. For the Si-O pair, they refer to distances in crystals with the same stoichiometry. We did not report the values for all compositions studied because we are interested here only in the effect of the inclusion of the different three-body interactions and the Li-O and K-O parameters in the two BMP potentials (which are independent of the glass composition) and in the differences between the potentials used.

The figure shows that, for all alkali disilicate glasses, the Si-BO PDF peak is centered at ∼1.61–1.64 Å, depending on the nature of the alkali cation and on the potentials. The first peak of the experimental TDF assigned to the Si-O bond length is centered at ∼1.63, 1.61, and 1.64 Å for LS33, NS33, and KS33 glasses, respectively. All potentials reproduce well this peak, but slightly different bond lengths are observed. PMMCS and SHIK potentials provide slightly smaller distances at ∼1.60–1.61 and 1.61–1.62 Å, whereas the CSM and the two BMP potentials provide slightly longer distances at ∼1.62–1.64 Å, depending on the alkali cation in the glass. Therefore, the introduction of the three-body potential leads to longer Si-O distances because of the increased repulsion between Si cations when narrower Si-O-Si angles are formed. This effect is more evident by looking at the Si-BO PDFs reported in Fig. 4, which shows an elongation of 0.02 Å for this bond with BMP-harm and of 0.03 Å with BMP-shrm;

in fact, the latter potential generates narrower Si-O-Si angles with respect to the former one. On the contrary, the Si-NBO bond lengths slightly reduce by 0.01 Å. Consequently, the difference between the Si-BO and Si-NBO bonds increases to ∼0.08–0.09 Å, in good agreement with the difference observed in the disilicate crystals [57], which are reported as vertical lines in the figure. In general, the CSM and SHIK potentials provide smaller differences between the length of the Si-BO and Si-NBO bonds, especially for the LS33 and KS33 glasses.

Regarding the alkali cation-oxygen distances, the two BMP potentials always provide the same values, with a perfect overlapping of the PDFs because they share the same alkali cation-oxygen parameters. We observe that the first peak of the Li-O PDFs is centered at different distances for the different potentials. The SHIK potential provides the shorter average distances (computed by averaging the distance values at half of the peak height) of 1.86 Å, followed by both the BMPs (1.91 Å), the CSM (1.91 Å), and PMMCS (2.01 Å). A neutron diffraction isotopic substitution study of the $Li_2Si_2O_5$ glass reported the value 1.97 Å [58]. As for the Na-O PDF, we observed that the SHIK and CSM potentials provide similar shapes and positions with a first peak more intense and narrower with respect to that of the PMMCS and the two BMP potentials, which are the same since they share the same parameters. The average Na-O bond distances are ∼2.30, 2.32, and 2.34 Å for SHIK, CS, and PMMCS

TABLE III. Experimental and simulated P-NBO, P-BO, and P-P distances, where NBO and BO stand for nonbridging oxygen and bridging oxygen, respectively, for all studied potentials.

Glass	Experimental (Å)			PMMCS (Å)			Core-shell (Å)			BMP-harm (Å)			BMP-shrm (Å)		
	P-NBO	P-BO	P-P	P-NBO	P-BO	P-P	P-NBO	P-BO	P-P	P-NBO	P-BO	P-P	P-NBO	P-BO	P-P
NP	1.48	1.61	2.93	1.50	1.56	3.10	1.50	1.60	3.07	1.47	1.58	2.97	1.47	1.58	2.97
CP	1.49	1.6	2.94	1.50	1.56	3.09	1.50	1.60	3.04	1.48	1.57	2.97	1.48	1.58	2.97
NCP	1.49	1.6	2.93	1.50	1.56	3.09	1.50	1.60	3.04	1.48	1.58	2.98	1.48	1.58	2.97

and 2.34 Å for both the two BMP potentials (which show the same value), respectively. These values fall well within the range (2.30–2.36 Å) found in experimental investigations [4,59]. As for the K-O PDFs, it is interesting to note that the ones obtained with the two BMP and CSM potentials are perfectly superimposable, whereas those computed with the SHIK and PMMCS potentials are similar. The average K-O bond distances are 2.64 Å for both the BMPs and the CSM, 2.72 Å for PMMCS, and 2.71 Å for SHIK potentials. Neutron diffraction experiments carried out by Hannon *et al.* [5] on the $(SiO_2)_{0.739}$-$(K_2O)_{0.261}$ glass provided K-O distances of 2.667 Å.

Moving to the aluminosilicate glasses, we observe that the Si-O PDFs are like the ones discussed for the alkali silicate glasses, and thus, they have not been reported here. Compared with Si-O, the peak of Al-O is broader, with a smaller amplitude, and it is centered at a larger r value of 1.74–1.77 Å, depending on the potentials. The CSM, PMMCS, and both the BMP potentials (that share the same Al-O parameters and provide the same PDFs) provide average bond distances at around 1.74 Å shorter than SHIK. The BMPs provide slightly longer (0.01 Å) Al-O distances. These bond lengths agree with *ab initio* simulations and experimental results, which showed Al-O distance of 1.71 and 1.77 Å, respectively [60,61].

Table III reports the experimental [54] and computed P-O and P-P distances for the binary phosphate glasses. P-NBO distances are overestimated by 0.01–0.02 by PMMCS and CSM FFs, while both the BMPs predict lower values of 0.01 compared with experiments. P-BO distances are well estimated by the CSM potential, while they are underestimated by 0.02–0.03 and 0.04–0.05 by the two BMPs and PMMCS potentials, respectively. P-P distances are greatly overestimated by PMMCS and the CSM, while both the BMPs predicts closer distances, confirming that the presence of the P-O-P three-body interaction, with the repulsive P-P one, allows a better evaluation of the intermediate-range structure.

D. *T*-O-*T* BADs

The *T*-O-*T* (*T* = Si, P, Al) BAD plays a key role in the description of the medium-range order of glasses. In previous papers [34,38], we demonstrated that the *T*-O-*T* BAD strongly affects the shape of the NMR spectra. In particular, the narrower angle provided by CSM potentials, which is a consequence of the inclusion of the polarization effects for oxygen ions, improves the agreement between experimental and simulated NMR spectra. Furthermore, it has been recently proposed that Si-O-Si angle distribution also affects the estimation of the ionic conductivity of glasses, allowing a

better explanation of the mixed alkali effect in aluminosilicate glasses [40], as it will be also shown in next paragraphs.

Figure 5 reports, as an explanatory example, the BADs of a few glasses for some *T*-O-*T* angles. All Si-O-Si BADs for all binary silicate glasses and, for example, the Si-O-P BAD comparison between PMMCS and the two BMP potentials for the NCPS_2.93 glass can be found in Figs. S4 and S5 of the Supplemental Material [43], respectively. The inclusion of the Si-O-Si, P-O-Si, and P-O-P three-body interaction in the two BMP potentials clearly impacts the distribution of these angles, shifting the peaks to lower values and narrowing them in comparison with those calculated with PMMCS. This effect is particularly evident when the screened harmonic three-body potential is used. In fact, BMP-shrm provides narrower Si-O-Si, P-O-Si, and P-O-P BADs, which are centered at smaller angles.

Different behaviors of the potentials are observed for the simulation of Si-O-Si distribution in *v*-silica, binary silicates, and aluminosilicate glasses. PMMCS and SHIK FFs always predict broader distributions, while the two BMPs and the CSM predict narrower ones. As for *v*-SiO_2, the availability of experimental Si-O-Si BAD allows us to perform a direct comparison with simulated data [62]. BMP-harm shows the best agreement with experiments, both for the shape and the position of the curve. BMP-shrm provides a slightly narrower curve, like the experimental one, although shifted to lower values. The other tested potentials show broader BADs, with the shape of the distribution different to experiment. The experimental average Si-O-Si angle provided by Charpentier *et al.* [63] is 147.1°, but other experiments and *ab initio* calculations provide values between 136° and 152° [64]. The average values obtained in this paper are 146.2°, 148.1°, 144.9°, 144.8°, and 149.9° for BMP-harm, SHIK, BMP-shrm, CSM, and PMMCS.

The average angles of LS30, NS30, and KS30 obtained with the different potentials are 150.5°, 150.8°, and 151.7° with PMMCS; 142.1°, 141.6°, and 141.2° with SHIK; 142.3°, 141.0°, and 141.2° with the CSM; 143.3°, 143.1°, and 143.0° with BMP-harm; and 139.9°, 139.8°, and 140.1° with BMP-shrm. All potentials, especially the PMMCS, overestimate these values for LS30 and NS30 with respect to the ones calculated from *ab initio* calculations [65] (133.6° and 135.2°, respectively), and BMP-shrm provides the closer values. As for KS30 glass, good average angles close to the *ab initio* ones (141.2°) are provided by SHIK (141.2°), the CSM (141.2°), BMP-harm (143.0°), and BMP-shrm (140.1°), but not by PMMCS (151.7°). All potentials show a decrease in the position of the maximum of the Si-O-Si BAD when the content of the modifier increases (see Fig. S4 of the Supplemental Material [43]), in agreement with experimental data
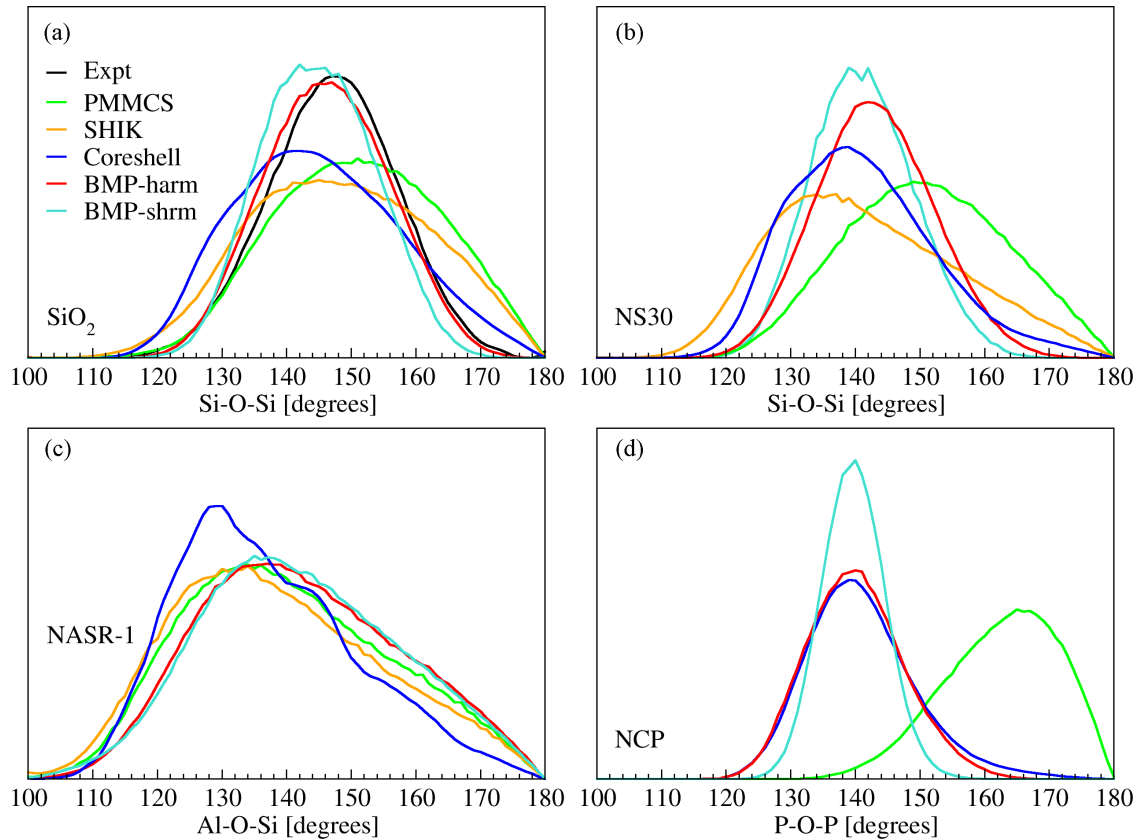
FIG. 5. Si-O-Si, Si-O-Al, P-O-P bond angle distributions in (a) v-silica, (b) binary alkali silicate NS30, (c) aluminosilicate NASR-1, and (d) sodium calcium phosphate NCP glasses.

[66]. The CSM is the only potential that shows a double peak in the Si-O-Si distribution of the KS series, which becomes more evident when the amount of K_2O in the glass increases. The position of the maximum obtained with SHIK and BMP-shrm are more in agreement with the CSM than that obtained with the BMP-harm. However, the shape of the BAD obtained with BMP-harm is more like the one observed with the polarizable model. As for the Al-O-Si distribution, CSM shows the narrower one, but still very broad if compared with Si-O-Si, with maximum around 129°. Here, the position of the maximum obtained with SHIK ($\sim$130°) is very close to the CSM, while PMMCS and the two BMPs show higher values of 133° and 137°, respectively. Reasonably, the repulsive interaction between Al and Si leads to a slight increase in the Al-O-Si bond angle. Concerning the P-O-P angle distribution, the inclusion of the P-O-P three-body interaction strongly affects its position and shape, narrowing and shifting it to much lower values, as the position of the maximum is around 166° for PMMCS and 140° for both the BMPs. In this case, the BAD obtained with the CSM and BMP-harm are almost superimposable, while BMP-shrm provides a much narrower and higher peak.

E. Q^n distributions

Si-O, P-O, and Al-O bonds present a mixture of covalent and ionic natures, whose balance strongly depends on the local coordination, specifically on the intertetrahedral connectivity and on the geometry and amount of modifier ions in the

local environment of SiO_4, PO_4, and AlO_4 units. Therefore, in principle, a very accurate FF should consider the specific local environment of ions in the calculation of the interactions between atoms [67,68]. The CSM, with its explicit inclusion of polarization, allows the model to respond to the local fluctuation of the electric field caused by the ionic motion, while RIMs, even with the inclusion of the partial covalence of the bond through the employment of partial charges, may not fully reproduce the various local environment of network former ions [32]. Although it does not allow us to include polarizability, the inclusion of T-O-T (T = Si, P) three-body potentials partially overcome the problems caused by the RIMs, leading to a better estimation of the network connectivity, represented by the Q^n speciation of the network-former atoms, as shown in the following paragraphs.

1. Silicon

Figure 6 shows the Si (Q^n) speciation of binary silicate glasses computed with all studied potentials compared with experimental data obtained by deconvolution of ^{29}Si NMR spectra [69–72]. All potentials follow the experimental trends.

Unsurprisingly, the CSM FF provides the best agreement with NMR derived data with MAEs of 4.8%, 5.8%, and 12.2% for the LS, NS, and KS series, respectively, confirming what we expected initially. Comparing the RIMs, the BMP-shrm potential systematically provides data closest to experiments, especially at high concentration of the modifier, showing both better absolute values and trends with MAEs of 5.7%, 8.1%,
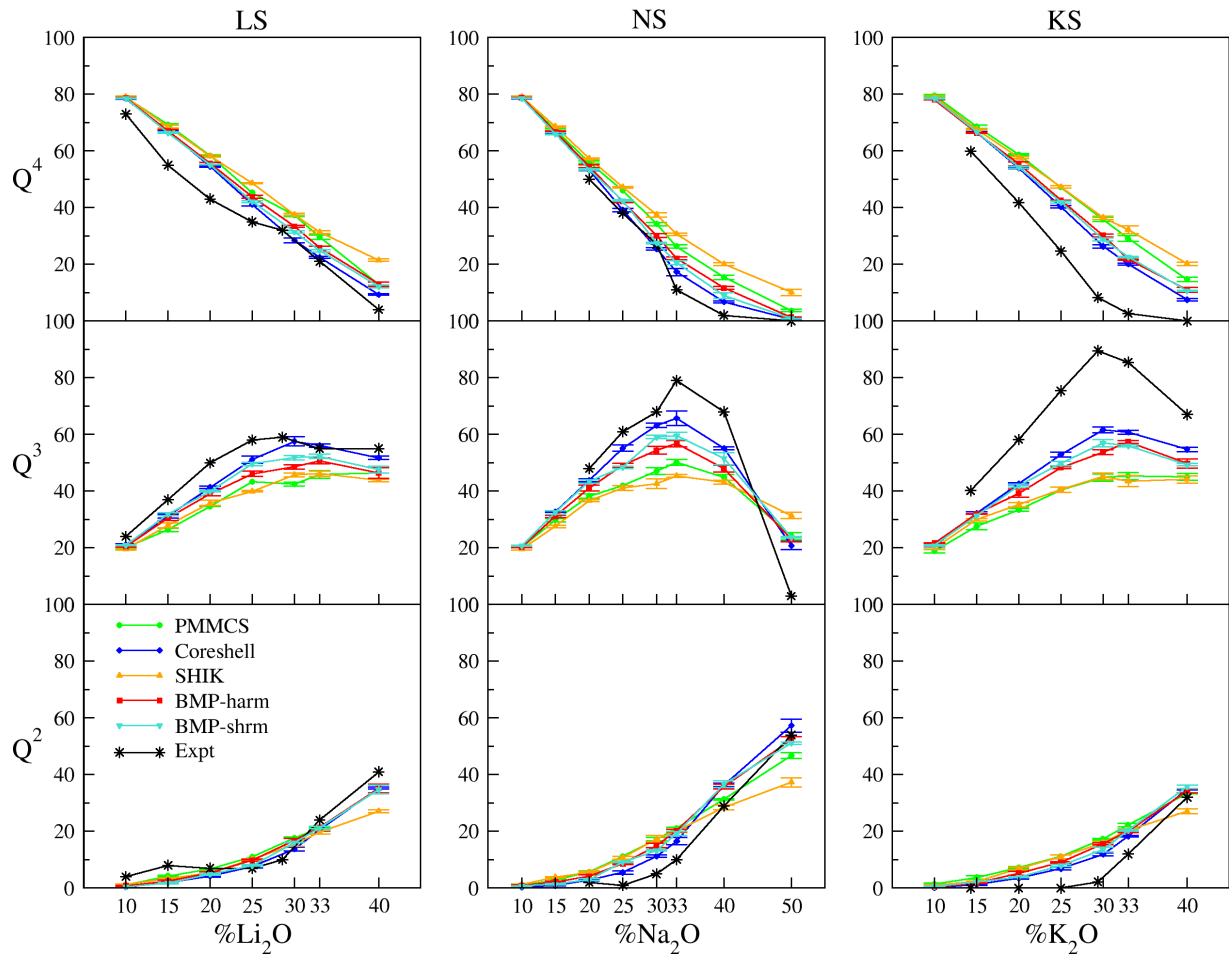
FIG. 6. Computed and experimental trends of the Q^n species in the alkali silicate glasses investigated.

and 14.2% for the LS, NS, and KS series, respectively, followed by BMP-harm, which shows MAEs of 6.7%, 9.3%, and 14.7%. PMMCS gives a worse agreement with the experiment compared with the two BMP potentials, with MAEs of 8.5%, 12.4%, and 19.2%, for LS, NS, and KS, respectively, confirming the improvement led by the inclusion of the three-body interactions. The SHIK FF always provides the worst agreement, exhibiting MAEs of 9.2%, 15.1%, and 19.4%.

Figure S6 of the Supplemental Material [43] displays the Si (Q^n) speciation in the NCPS_2.11 glass, often named as 45S5 Bioglass [73], calculated with the CSM, PMMCS, and the two BMP potentials compared with experimental data [72]. BMP-shrm provides the best agreement with the experimental data (MAE = 5.9%), especially for the Q^1 and Q^2 fractions, followed by the CSM (MAE = 6.3%) and BMP-harm (MAE = 7.6%).

2. Phosphorus

The P (Q^n) speciation in the sodium-calcium phosphate glasses obtained with the studied potentials is reported in Fig. 7(a). Experimentally [74], from ^{31}P MAS spectra, only chains made by Q^2 species were found in NP glass, while a small amount of Q^1 (4% in CP) is present in calcium-bearing glasses, probably because of the partial hydrolysis of the structure, which is known to occur in phosphate glasses [75].
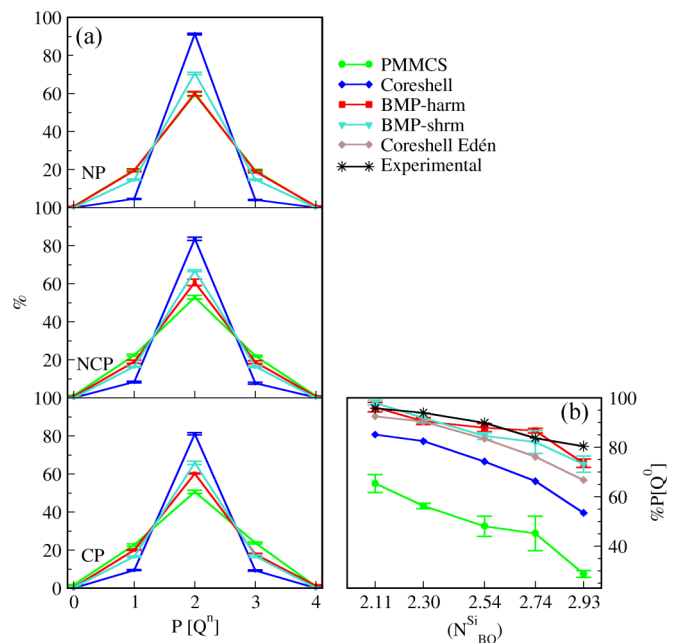

FIG. 7. (a) Phosphorous Q^n distributions in NP, NCP, and CP glasses; (b) trends of the Q^0 species for phosphorous in phosphosilicate glasses for BMP-harm, BMP-shrm, PMMCS, and two core-shell model (CSM) parameterizations.

The CSM potential provides the best agreement with experiments, giving percentages of Q^2 species between 79% and 90% and very small fractions of Q^1 and Q^3, which increase when Ca substitutes Na in the glass composition. BMP-shrm gives the best values concerning the RIMs (Q^2 values from 65% to 70%), especially for the NP glass, for which the percentage of Q^2 species increases by 11 points, getting closer to CSM quality. BMP-harm shows an improvement of the quality of data with respect to PMMCS in the CP and NCP glasses, while the two potentials give almost the same results for the NP. Another important feature of the P (Q^n) speciation is the orthophosphate [P (Q^0)] fraction over the Si network connectivity (defined as the average BO per Si atom and denoted N_{BO}^{Si}) in NCPS glasses in the range $2.0 \leqslant N_{BO}^{Si} \leqslant 3.0$ with $P_2O_5 \leqslant 6\%$, as it is an important parameter for the evaluation of MD models of bioactive glasses [76]. In this compositional regime, the P (Q^0) fraction decreases with the Si network connectivity but is independent of its P content [72].

Figure 7(b) reports the comparison between calculated and experimental [72] orthophosphate percentage over the Si network connectivity in the NCPS series. Here, we have reported, in addition to the FFs considered so far, also the CSM potential with the P-O parameter modified by Stevensson *et al.* [17], which shows better agreement with experimental data than the original one developed by Tilocca *et al.* [31].

Interestingly, the two BMP potentials show the best agreement with the experimental data (MAEs of 3.2% and 3.8% for BMP-harm and BMP-shrm, respectively), even closer than both the CSM potentials for all glass compositions (MAE of 6.9% for the Stevensson *et al.* [17] modification and 16.9% for the original Tilocca *et al.* [31] parameters), while PMMCS greatly underestimates the orthophosphate fraction in all glasses (MAE of 40.1%).

3. Aluminum

Figure 8(a) displays the percentage of NBO bonded to aluminum atoms and Fig. 8(b) the total percentage of NBO in the NAS*R* and NAS*T* glass series calculated with all studied potentials. Silicon and aluminum tetrahedra, in charge-balanced aluminosilicate glasses, are mostly polymerized to form mainly BO sites (Si-O-Si, Si-O-Al, and Al-O-Al), with only small amounts of NBO [6]. It is generally believed that sodium acts as a charge compensator for the negative AlO$_4$ units, and it does not break Al-O bonds to generate NBOs in this kind of glass. This statement is supported both by *ab initio* calculation [77] and experiments [78], where the Si-NBO bond is demonstrated to be more energetically favored than Al-NBO.

In the NAS*R* series, the Al/Na ratio is always one, so the percentage of NBO must be ~0. From this perspective, we can state that the CSM and the two BMP potentials are the only ones that always provide <5% NBO, while PMMCS always provides the highest one. All FFs predict a decreasing content of NBO in the NAS*R* series, paralleling the decreasing Na content. The CSM potential generally exhibits the lowest Al-NBO content (<5%), while SHIK always provides the highest [40]. Both the BMPs show high values for NAS*R*-0.7, where the percentage of Al$_2$O$_3$ is the highest, values under 9% for NAS*R*-1, and 0% for NAS*R*-3. As for the NAS*T* series, the
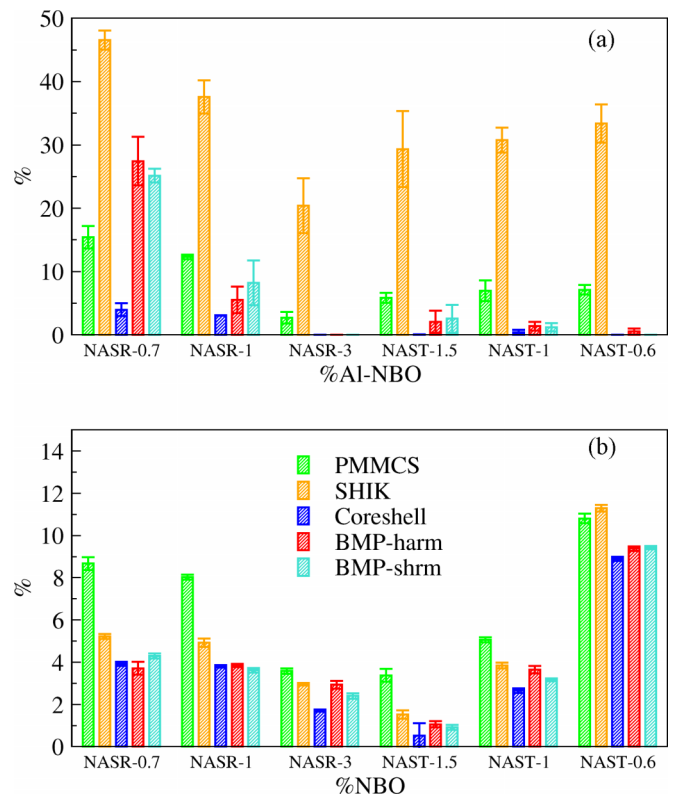

FIG. 8. (a) Percentage of NBO bonded to aluminum atoms and (b) total percentage of NBO in the NAS*R* and NAS*T* glasses calculated with all studied potentials.

decreasing of the Al/Na ratio leads to the formation of major amounts of NBOs. In the ipoalkaline glass NAS*T*-1.5, and in the charge-balanced NAS*T*-1, the amount of NBO must, theoretically, be ~0, as all the sodium can act as a charge compensator for the negatively charged AlO$_4$ units, while in the peralkaline glass NAS*T*-0.6, the excess of sodium acts as a network modifier and generates NBOs. This ideal trend is almost followed by all potentials, with the CSM providing the lowest values, followed by the two BMPs, and PMMCS providing the highest ones. In fact, the lowest NBO content is obtained for NAS*T*-1.5 and NAS*T*-1 (the latter shows values close to the NAS*R* series, as they share the same Na/Al ratio). The Al-NBO percentage provided by the two BMPs and the CSM is always ~0, while PMMCS and SHIK predict 5–7% and 29–34%, respectively, confirming the superiority of BMP potentials in the estimation of the short-range order around aluminum atoms with respect to the other RIMs tested.

F. Al/Si intermixing

The intermixing between Si and Al in the aluminosilicate glass frameworks is often described in terms of the Al avoidance or Loewenstein's rule [79], which states that Al-O-Si linkage is more favorable than the combination of Al-O-Al and Si-O-Si, and totally rejecting the existence of Al-O-Al linkages, if not required by composition ($R = Si/Al < 1$). Nevertheless, evidence of the presence of Al-O-Al bridges in charge-balanced aluminosilicate glasses with Si/Al < 1 was found in ^{17}O 3QMAS NMR spectra with clearly resolved
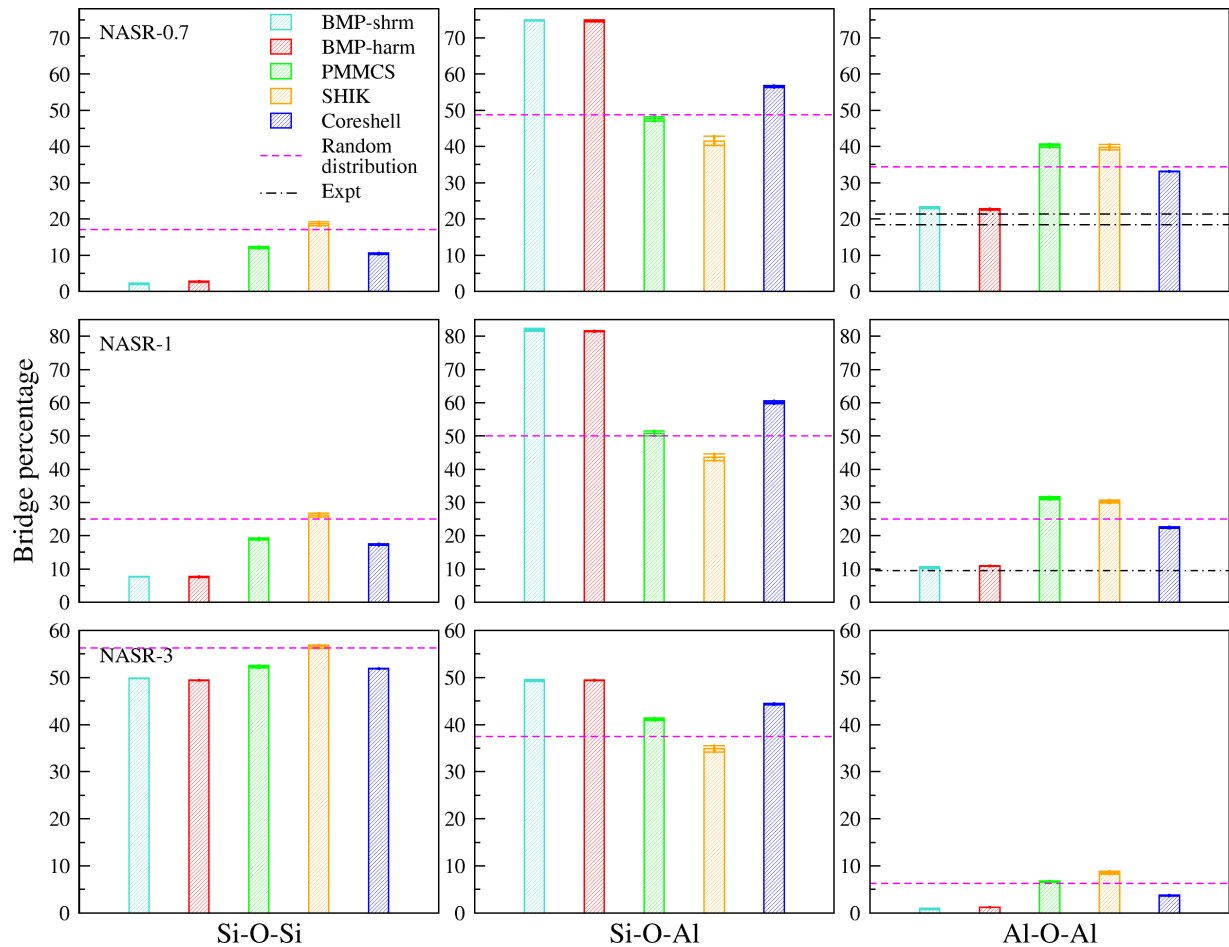
FIG. 9. Percentage of T_1-O-T_2 bridges (where T_1 and T_2 = Si, Al) in the simulated NASR glasses. The cyan and black horizontal lines highlight the values computed, assuming a random distribution of Al/Si species, and the one determined experimentally, respectively [6].

Al-O-Al peaks [80]. A complete Al avoidance rule would require that, in glasses with Si/Al = 1, only Al-O-Si bridges are present, and no Al-O-Al must be present for Si/Al > 1, but 3QMAS ^{17}O NMR studies on these kinds of glasses clearly show resolved Si-O-Si and Al-O-Al sites in spectra of glasses with $R = 1$, directly demonstrating the imperfectness of Loewenstein's rule [81]. The population of these sites represents the extent of disorder of the network-former cations and affects the properties of melts, such as heat capacity, entropy, silica activity, and viscosity [82].

Figure 9 reports the percentage of T_1-O-T_2 bridges (where T_1 and T_2 = Si, Al) in the simulated NASR glasses. Experimental values for the Al-O-Al linkage and data calculated from completely random distribution structures are also showed as dashed black and magenta horizontal lines.

All tested potentials predict an increasing (Si-O-Al)/(Al-O-Al) ratio, mainly due to a decrease of Al-O-Al linkages, with increasing R, in agreement with experimental data [6]. Al-O-Al percentages obtained with both BMP potentials, the lower computed values for all studied glasses, followed by the ones obtained with the CSM potential, show the best agreement with experimental data, highlighted by the black dashed horizontal lines in the right panels of Fig. 9.

Moreover, the BMPs predict the higher Al-O-Si percentage for all glasses, favoring the intermixing between the two

cations, as expected by Loewenstein's rule. The CSM also predicts Al-O-Si percentages always higher than the one predicted by the complete random distribution, while the SHIK potential always shows lower values. Opposite trends can be found for the Si-O-Si bridges, where the BMP and CSM potentials predict the lower percentages, SHIK the higher, and PMMCS stays in the middle.

G. NMR spectra

NMR spectroscopy is a particularly powerful tool for the investigation of glass structures, as its signal depends on the local environment of the active nuclei, enabling us to obtain precise information on both the short- and medium-range order around them. For this reason, a good way to validate a simulated model and, consequently, the FF used to generate it is the comparison between simulated and experimental NMR spectra. In fact, if good agreement is achieved, it is reasonable to assume that the local environment around the investigated nuclei of the simulated model is like the real one.

Figure 10 shows the experimental [6,69,70,74,83–86] and calculated ^{17}O, ^{27}Al, ^{29}Si, and ^{31}P NMR spectra of the NS33, NASR-1, and NCPS_2.11 glasses.

Panel (a) of the figure clearly shows that the inclusion of the three-body interaction in the two BMP potentials, specif-
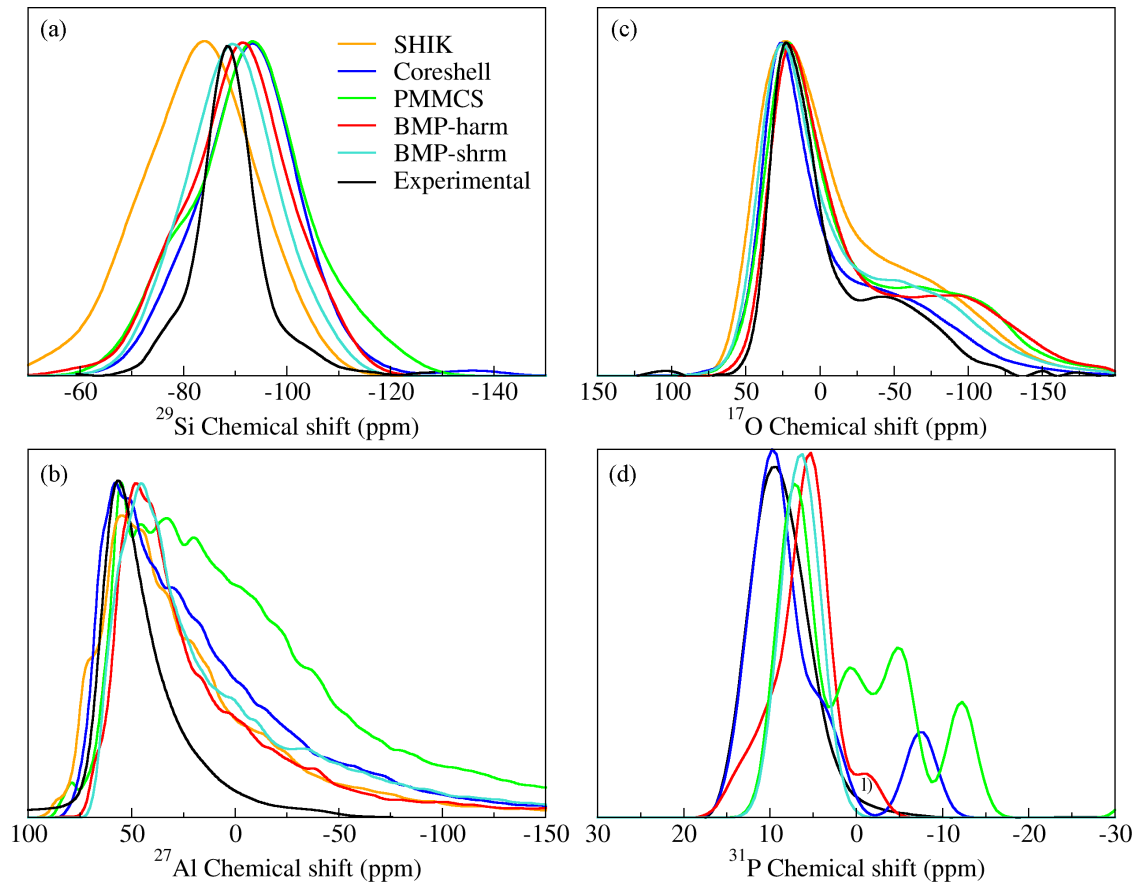
FIG. 10. Simulated and experimental MAS NMR spectra of (a) ^{29}Si of NS33, (b) ^{27}Al of NASR-1, (c) ^{17}O of NS33, and (d) ^{31}P of NCPS_2.11 glasses.

ically the screened harmonic one, leads to an improvement in the simulation of ^{29}Si spectra of silica-based glasses [see Fig. 10(a)]. BMP-shrm reproduces spectra in best agreement with experimental data, both in terms of peak positions and spectral shape. BMP-harm provides good spectra, showing an improved position and shape of the peaks with respect to PMMCS, which exhibits broader spectra, positioned at slightly lower chemical shift, sharing the same position with the CSM. The SHIK potential provides broader signal positioned at slightly higher chemical shifts.

The ^{17}O MAS NMR spectrum of the NS33 glass [Fig. 10(c)] is well reproduced by all FFs. The CSM predicts the best spectra, while SHIK provides the broader ones. BMP-shrm provides slightly better agreement with experiment with respect to BMP-harm, especially in the shape and position of the shoulder of the ^{17}O signal at lower chemical shifts, associated with BOs, in the alkaline silicate glasses. This is ascribed to a better estimation of the Q^n species and Si-O-Si BAD.

Regarding the ^{27}Al NMR spectra of NASR-1 glass, the improvement from PMMCS to both the BMPs is particularly evident [Fig. 10(b)]. The two BMP potentials do not show significant differences but just a slightly narrower peak for the BMP-harm, and they provide, with the SHIK potential, the narrowest peaks, even narrower than the one obtained with the CSM potential, with a slightly underestimated position ($\sim$10 ppm). However, the SHIK models shows a further peak

at higher chemical shifts caused by the presence of Al ions bearing NBOs.

As for the ^{31}P MAS spectrum, it is well known that the signal of ^{31}P strongly relies on the Q^n speciation of phosphorus [87]. The experimental ^{31}P MAS spectrum [Fig. 10(d)] of the NCPS_2.11 glass shows a single, well-resolved peak at $\sim$9 ppm assigned to the dominant Q^0 species in this glass. The shape of this spectrum is well reproduced by the CSM, BMP-harm, and BMP-shrm potentials, with the latter providing the narrowest signal. The BMP-harm and CSM potentials exhibit a little second peak at lower chemical shifts, due to a small fraction of Q^1 species, while PMMCS provides a very broad and badly resolved peak caused by the relatively high amount of Q^1 species in the models and the very broad P-O-P BADs shown previously.

It is worth noting that, in this paper, we did not optimize the geometry of the simulated models at the DFT level before calculating the NMR spectra to highlight differences between the studied potentials. This kind of optimization fairly improves the position of the signals in simulated NMR spectra, optimizing atom distances to minimize forces with DFT accuracy. If this technique had been applied, a better agreement would have probably been achieved between experimental and simulated spectra and between the ones obtained with RIM and CSM FFs.

Summarizing, the inclusion of the T-O-T (T = P, Si) three-body interactions strongly improves the agreement between calculated and experimental NMR spectra. Since it is known
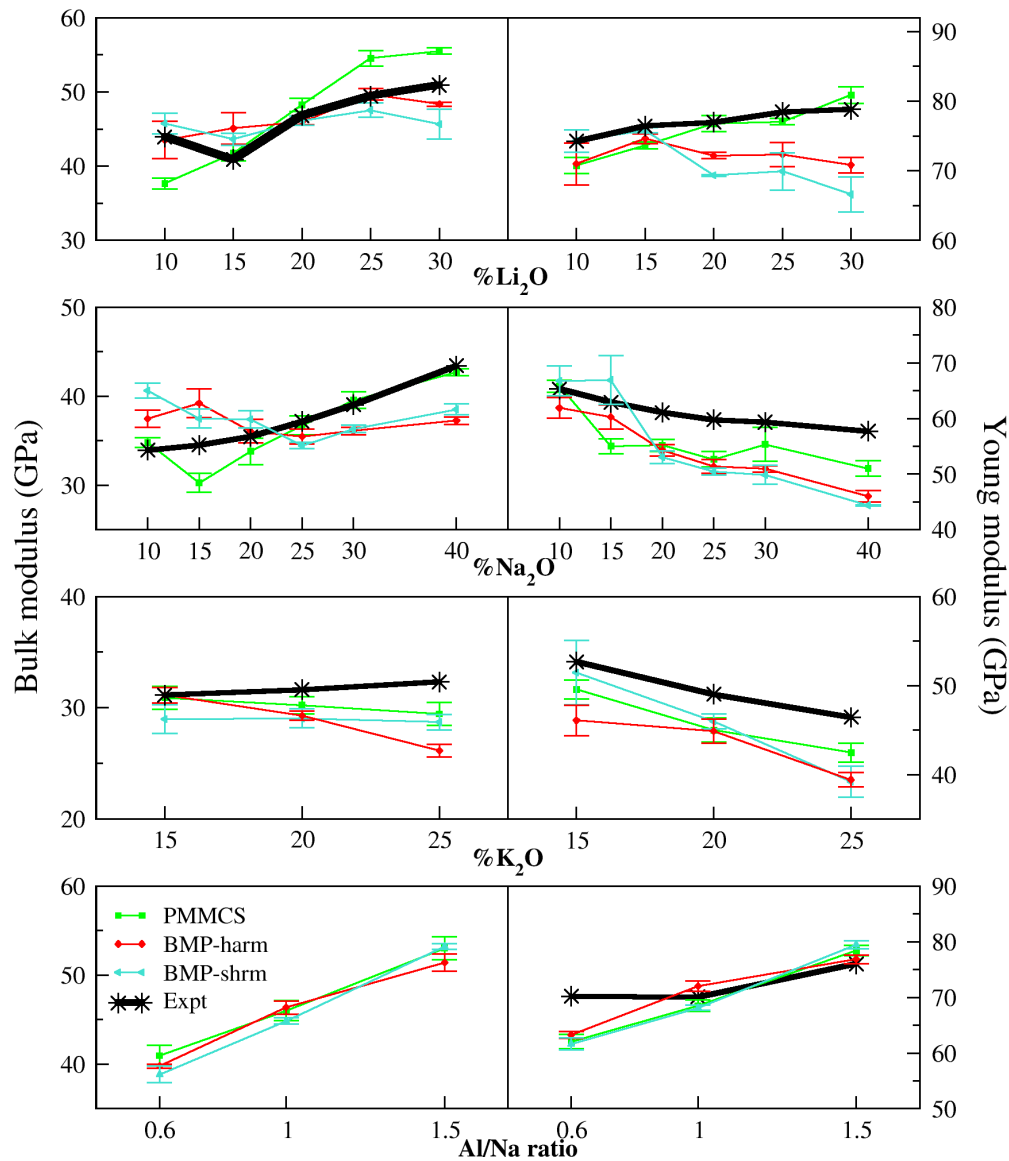
FIG. 11. Elastic constants (Young's modulus, shear modulus, and bulk modulus) of the binary alkali silicates and sodium aluminosilicate NAST glasses computed with the different potentials. The mean absolute error (MAE) has been calculated for all properties. They are MAE$_{PMMCS}$ = 2.53, MAE$_{BMP-harm}$ = 3.42, and MAE$_{BMP-shrm}$ = 3.74 for the bulk modulus, and MAE$_{PMMCS}$ = 3.96, MAE$_{BMP-harm}$ = 5.60, and MAE$_{BMP-shrm}$ = 5.86 for the Young modulus.

that a correlation exists between the isotropic chemical shift of the network former and the T-O-T angles and this has been exploited to map out the T-O-T BADs from the NMR spectra [34,62,88], it seems reasonable to assume that the models generated with the FFs reproduce reliably the T-O-T BADs.

H. Elastic Properties

The capability of the two BMPs and the PMMCS FFs to reproduce the elastic properties of multicomponent oxide glasses has been tested using the LS, NS, KS, and NAST glass series for which the experimental values of the bulk and Young's moduli are available in the literature [53,89].

The elastic properties have been computed using the static method described in sec. 2.2.1 of the Supplemental Material [43]. Here, we report only the data obtained with the PMMCS

and BMP potentials to highlight the differences between the original and the revised parametrization. A comparison of the Young modulus calculated by straining the specimens during MD simulations with PMMCS, BMP-harm, BMP-shrm, and SHIK potentials has also been reported in sec. 2.2.2 of the Supplemental Material [43].

The computed and experimental data values for these glasses are reported in Fig. 11.

In general, the bulk modulus of the binary silicate glasses increases with alkali content; the increment is more evident for lithium than sodium and potassium. All FFs reproduce well this trend for the LS and NS series, even if the PMMCS seems to perform slightly better for the NS one, while BMP-harm for LS. Instead, none of them perfectly reproduces the monotonic trend of the KS series. PMMCS and BMP-harm show a decrement in the bulk modulus when K_2O content
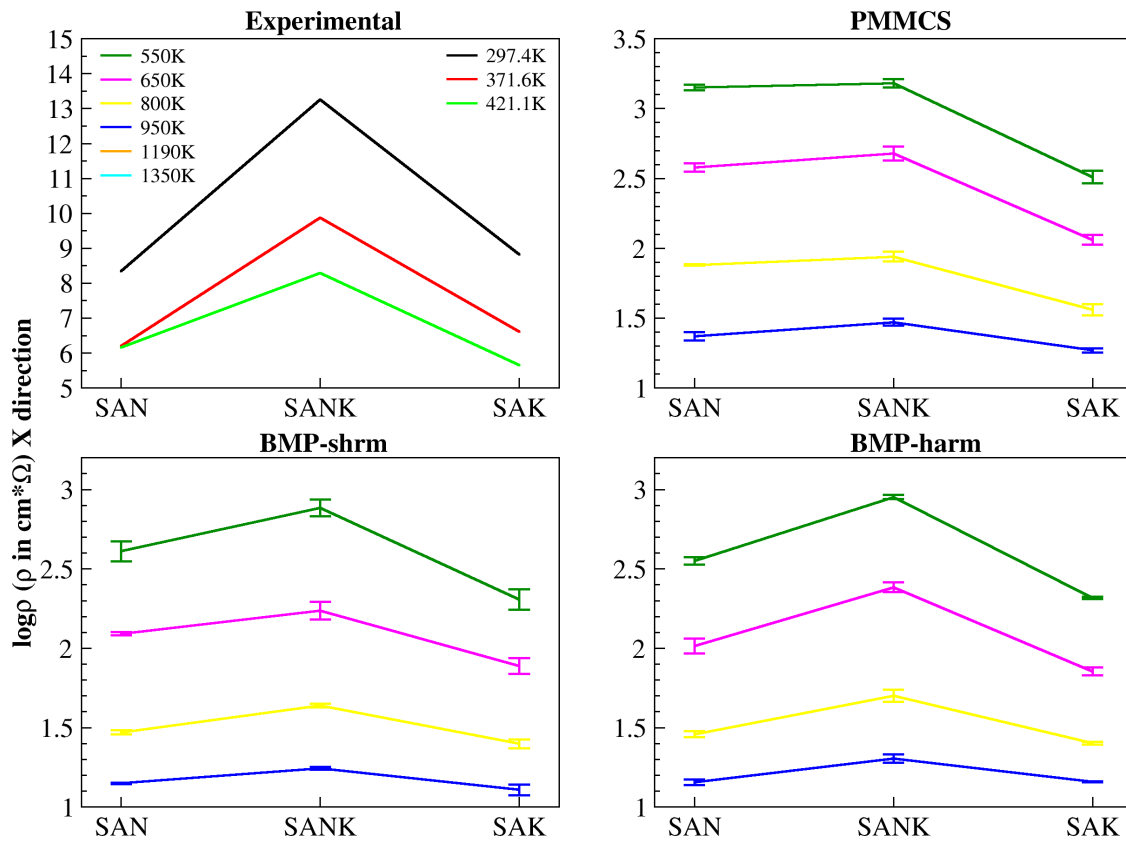
FIG. 12. Logarithm of resistivity obtained for the three glasses studied at variable temperature by different interatomic potentials.

increases, while BMP-shrm remains almost constant. The bulk modulus of silica is overestimated by all potentials, but PMMCS gives values closer to experiment. The PMMCS and BMP FFs reproduce well the descending trends observed for Young's modulus in the NS and KS series. This increase for the LS series is well followed only by PMMCS, while the BMPs show a slightly decrement.

Regarding the aluminosilicate glasses, we observe that all elastic constants increase with increasing alumina content (Al/Na ratio), as also observed experimentally [89]. This result agrees with the knowledge that the addition of alumina into silicate glass should always cause an increase in elastic modulus. All reported potentials give good results for the NAST-1 and NAST-1.5 glasses, while a larger error (up to 9 GPa) is found for NAST-0.6. For the aluminosilicates, the two BMPs and PMMCS FFs are equivalent in agreement with the fact that no Si-O-Al and Al-O-Al three-body interactions have been included in the potential set.

Overall, PMMCS results to be slightly better than the BMPs for the prediction of all considered elastic properties, as confirmed by the MAEs for all of them (caption of Fig. 11). As for the BMP potentials, the BMP-harm usually provides better agreement with experiments, giving for all studied properties a lower MAE of 0.4 than BMP-shrm.

In conclusion, the introduction of the Si-O-Si three-body potentials does not significantly worsen the ability of the BMP potentials to predict the mechanical properties of oxide glasses, which was one of the major strengths of the PMMCS potential [90].

I. Ionic conductivity and resistivity

The ability of the improved FFs to reproduce ionic conductivity has been tested using mixed Na-K aluminosilicate glasses named SAN, SANK, and SAK with composition $(25-x)Na_2O-xK_2O-10Al_2O_3-65SiO_2$ ($x = 0$, 12.5, and 25). These glasses present the so-called mixed alkali effect [91,92], a large nonlinear deviation in dynamical properties (diffusion, viscosity, chemical durability, and the glass transition temperature [93]) observed when an alkali cation is gradually replaced by another alkali cation. The ionic conductivity (resistivity) of glasses exhibiting this effect shows a deep minimum (maximum) when half of the alkaline ions of type A are replaced by type B ions, meaning that cation mobility progressively reduces up to a substitution ratio equal to unity. The minimum is more pronounced at low temperatures, where the activation energy for ionic diffusion has a maximum, and it usually reduces increasing the temperature. This phenomenon has been deeply investigated experimentally and computationally, and it has been explained by the suppression of jump events of the alkaline ions between dissimilar sites in the percolation channels hosting both A and B ions [94–97].

In a recent paper [40], we benchmarked the PMMCS, Deng and Du [14], Guillet and Sator [16], SHIK, and CSM potentials and found that the latter model is the only one able to reproduce the alkaline mixing effect in the ionic conductivity of the abovementioned Na, K aluminosilicate glasses. Figure 12 reports the resistivity data computed at

different temperatures using the PMMCS and our two BMP parameterizations.

Interestingly, both BMP parameterizations can reproduce well the mixed alkali effect on the ionic conductivity. A rationalization of the reason for the trends observed for the different potentials can be found in a deep analysis of the microstructure of the glasses, as showed in our previous paper [40].

We have observed that the PMMCS potentials provide structures (in terms of coordination numbers and Al/Si and K/Na intermixing) like the ones obtained with the CSM potential, but they develop different bond angles and ring size distributions which have a profound impact on the way the modifier cations are accommodated in the percolation channels.

As highlighted in the previous sections, the introduction of the three-body interactions in the two BMP potentials shift to narrower Si-O-Si angles and greater average ring sizes with the addition of K cations. In fact, the average ring sizes obtained using the CSM increase from 8.0 to 8.3 and 8.5 going from SAN to SANK and SAK glasses. With the PMMCS, the average ring sizes assume a constant value of eight silicon atoms per ring independently on the K content. When the BMP-harm potential is used, the average ring sizes are 8.3, 8.5, and 9.0, while when BMP-shrm is used, they are 8.2, 8.6, and 9.0, for SAN, SANK, and SAK glasses, respectively. This corroborates our previous statements that, to accommodate larger cations in the percolation channels, the rings must contain more tetrahedral units if the intertetrahedral angles are reduced [40].

V. CONCLUSIONS

A generation of the PMMCS FF has been presented. Improvements in the performances have been achieved by including (i) two different kinds of T-O-T (T = Si and P) three-body interactions, specifically, harmonic and screened-harmonic functional forms; (ii) Si-Si, Si-Al, Si-P, Al-Al, and P-P repulsive interactions; and (iii) refined Li-O, K-O, and P-O pairwise parameters. The FFs, named BMP-harm and BMP-shrm, reproduce structure and properties of silicates, aluminosilicate, phosphate, and phosphosilicate glasses significantly better than the previous one.

The ability of the FFs to reproduce smaller and narrower T-O-T BADs leads to a better prediction of the intermediate-range structure (Q^n distributions, Al/Si intermixing, and partitioning of the NBOs), ^{29}Si, ^{27}Al, ^{31}P, and ^{17}O MAS

NMR spectra, and ionic conductivities of multicomponent oxide glasses with respect to the PMMCS FF. Therefore, the T-O-T BAD seems to be an important structural feature in oxide glasses. Unfortunately, the experimental determination is difficult, and one could argue that the right distribution is unknown. However, it is known that a correlation exists between the isotropic chemical shift of the network former and the T-O-T angles, and this has been exploited to map out the T-O-T BADs from the NMR spectra [34,62,88]. Therefore, we assume that models able to reproduce well the NMR spectra subtend a reliable T-O-T BAD.

Whereas the properties are reproduced with similar accuracy, BMPs outperform the current parameterization of the CSM for the prediction of densities and elastic constants. On the contrary, no improvements are observed for the vibrational density of states (see sec. 3.6 in the Supplemental Material [43]), which is reproduced similarly to the PMMCS FF. Previous investigations showed that accurate results can be reached using the CSM [37,98], suggesting that polarizability effects not included in our FFs are necessary in this respect. It should be noted that vibrational frequencies were not used to optimize the BMP FF, and thus, we cannot be sure that it is the polarizability that improves these properties as for the dielectric properties which instead by definition depend on it. However, the way in which the CSM includes the polarizability seems to affect the Si-O-Si angle and, thus, the intermediate-range order. Unfortunately, it is not possible to quantify the correlations among them, and a definitive answer to the second question posed in the introduction is not reached.

Among the BMP potentials, the screened BMP-shrm estimates better the intermediate-range order around Si and P and, thus, their MAS NMR spectra, whereas they perform similarly for the other properties.

Obviously, the inclusion of three-body interactions reduces the computational efficiency of the BMP with respect to PMMCS. With the same computational setting and system size, the integration of the equations of motion for the same period requires a computational time 2 and 10 times higher for the BMP and CSM FFs, respectively. Another strength of our FFs is that they include parameters for the interactions of many elements of the periodic table in different ionic states of the oxide ions and, thus, allow a consistent investigation of multicomponent oxide glasses. Work is ongoing in our research group to extend the BMP FFs for boron-containing glasses to enlarge their applicability to these fascinating systems.

[1] J. C. Mauro, C. S. Philip, D. J. Vaughn, and M. S. Pambianchi, Glass science in the United States: Current status and future directions, Int. J. Appl. Glass Sci. **5**, 2 (2014).

[2] L. Li, H. Lin, S. Qiao, Y. Zou, S. Danto, K. Richardson, J. D. Musgraves, N. Lu, and J. Hu, Integrated flexible chalcogenide glass photonic devices, Nat. Photonics **8**, 643 (2014).

[3] A. K. Varshneya, *Fundamentals of Inorganic Glasses*, (Gulf Professional Publishing, New York, 1994) .

[4] G. N. Greaves, A. Fontaine, P. Lagarde, D. Raoux, and S. J. Gurman, Local structure of silicate glasses, Nature **293**, 611 (1981).

[5] A. C. Hannon, B. Vessal, and J. M. Parker, The structure of alkali silicate glasses, J. Non-Cryst. Solids **150**, 97 (1992).

[6] S. K. Lee and J. F. Stebbins, The structure of aluminosilicate glasses: high-resolution ^{17}O and ^{27}Al MAS and 3QMAS NMR study, J. Phys. Chem. B **104**, 4091 (2000).

[7] A. Pedone, Properties calculations of silica-based glasses by atomistic simulations techniques: a review, J. Phys. Chem. C **113**, 20773 (2009).

[8] J. Du, Challenges in molecular dynamics simulations of multi-component oxide glasses, in *Molecular Dynamics Simulations of Disordered Materials: From Network Glasses to Phase-Change Memory Alloys*, edited by C. Massobrio, J. Du, M. Bernasconi, and P. S. Salmon (Springer International Publishing, Cham, 2015), pp. 157–180.

[9] A. Pedone and M. C. Menziani, Computational modeling of silicate glasses: a quantitative structure-property relationship perspective, in *Molecular Dynamics Simulations of Disordered Materials: From Network Glasses to Phase-Change Memory Alloys*, edited by C. Massobrio, J. Du, M. Bernasconi, and P. S. Salmon (Springer International Publishing, Cham, 2015), pp. 113–135.

[10] Y.-J. Hu, G. Zhao, M. Zhang, B. Bin, T. Del Rose, Q. Zhao, Q. Zu, Y. Chen, X. Sun, M. de Jong, and L. Qi, Predicting densities and elastic moduli of SiO_2-based glasses by machine learning, Npj Comput. Mater. **6**, 1 (2020).

[11] K. Yang, X. Xu, B. Yang, B. Cook, H. Ramos, N. M. A. Krishnan, M. M. Smedskjaer, C. Hoover, and M. Bauchy, Predicting the Young's modulus of silicate glasses using high-throughput molecular dynamics simulations and machine learning, Sci. Rep. **9**, 8739 (2019).

[12] A. Pedone, G. Malavasi, M. C. Menziani, A. N. Cormack, and U. Segre, A new self-consistent empirical interatomic potential model for oxides, silicates, and silica-based glasses, J. Phys. Chem. B **110**, 11780 (2006).

[13] S. Sundararaman, L. Huang, S. Ispas, and W. Kob, New interaction potentials for alkali and alkaline-earth aluminosilicate glasses, J. Chem. Phys. **150**, 154505 (2019).

[14] L. Deng and J. Du, Development of boron oxide potentials for computer simulations of multicomponent oxide glasses, J. Am. Ceram. Soc. **102**, 2482 (2019).

[15] A. Tilocca, N. H. de Leeuw, and A. N. Cormack, Shell-model molecular dynamics calculations of modified silicate glasses, Phys. Rev. B **73**, 104209 (2006).

[16] B. Guillot and N. Sator, A computer simulation study of natural silicate melts. Part I: low pressure properties, Geochim. Cosmochim. Acta **71**, 1249 (2007).

[17] B. Stevensson, Y. Yu, and M. Edén, Structure-composition trends in multicomponent borosilicate-based glasses deduced from molecular dynamics simulations with improved B-O and P-O force fields, Phys. Chem. Chem. Phys. **20**, 8192 (2018).

[18] B. G. Dick and A. W. Overhauser, Theory of the dielectric constants of alkali halide crystals, Phys. Rev. **112**, 90 (1958).

[19] A. Aguado, L. Bernasconi, and P. A. Madden, Interionic potentials from *ab initio* molecular dynamics: the alkaline earth oxides CaO, SrO, and BaO, J. Chem. Phys. **118**, 5704 (2003).

[20] J. Du and A. N. Cormack, The medium range structure of sodium silicate glasses: a molecular dynamics simulation, J. Non-Cryst. Solids **349**, 66 (2004).

[21] B. M. Al-Hasni and G. Mountjoy, A molecular dynamics study of the atomic structure of $_x(MgO)_{100-x}(SiO_2)$, J. Non-Cryst. Solids **400**, 33 (2014).

[22] F. Angeli, O. Villain, S. Schuller, S. Ispas, and T. Charpentier, Insight into sodium silicate glass structural organization by multinuclear NMR combined with first-principles calculations, Geochim. Cosmochim. Acta **75**, 2453 (2011).

[23] Y. Deng, C. Eames, J.-N. Chotard, F. Lalère, V. Seznec, S. Emge, O. Pecher, C. P. Grey, C. Masquelier, and M. S. Islam, Structural and mechanistic insights into fast lithium-ion conduction in Li_4SiO_4-Li_3PO_4 solid electrolytes, J. Am. Chem. Soc. **137**, 9136 (2015).

[24] M. E. McKenzie, S. Goyal, T. Loeffler, L. Cai, I. Dutta, D. E. Baker, and J. C. Mauro, Implicit glass model for simulation of crystal nucleation for glass-ceramics, Npj Comput. Mater. **4**, 1 (2018).

[25] L. B. Skinner, A. C. Barnes, P. S. Salmon, L. Hennet, H. E. Fischer, C. J. Benmore, S. Kohara, J. K. Richard Weber, A. Bytchkov, M. C. Wilding, J. B. Parise, T. O. Farmer, I. Pozdnyakova, S. K. Tumber, and K. Ohara, Joint diffraction and modeling approach to the structure of liquid alumina, Phys. Rev. B **87**, 024201 (2013).

[26] S. Urata, R. Ando, M. Ono, and Y. Hayashi, Molecular dynamics study on nano-particles reinforced oxide glass, J. Am. Ceram. Soc. **101**, 2266 (2018).

[27] S. M. Wood, C. Eames, E. Kendrick, and M. S. Islam, Sodium ion diffusion and voltage trends in phosphates $Na_4M_3(PO_4)_2P_2O_7$ (M = Fe, Mn, Co, Ni) for possible high-rate cathodes, J. Phys. Chem. C **119**, 15935 (2015).

[28] S. Urata, Y. Takato, and K. Maeda, Molecular dynamics investigation of the fracture mechanism of a glass-ceramic containing cleavable crystals, J. Am. Ceram. Soc. **102**, 5138 (2019).

[29] K. Konstantinou, P. V. Sushko, and D. M. Duffy, Structure and ionic diffusion of alkaline-earth ions in mixed cation glasses A_2O-$2MO$-$4SiO_2$ with molecular dynamics simulations, J. Non-Cryst. Solids **422**, 57 (2015).

[30] L. Linati, G. Lusvardi, G. Malavasi, L. Menabue, M. C. Menziani, P. Mustarelli, A. Pedone, and U. Segre, Medium-range order in phospho-silicate bioactive glasses: insights from MAS-NMR spectra, chemical durability experiments and molecular dynamics simulations, J. Non-Cryst. Solids **354**, 84 (2008).

[31] A. Tilocca, A. N. Cormack, and N. H. de Leeuw, The structure of bioactive silicate glasses: New insight from molecular dynamics simulations, Chem. Mater. **19**, 95 (2007).

[32] A. Tilocca, Short- and medium-range structure of multicomponent bioactive glasses and melts: An assessment of the performances of shell-model and rigid-ion potentials, J. Chem. Phys. **129**, 084504 (2008).

[33] R. I. Ainsworth, D. D. Tommaso, J. K. Christie, and N. H. de Leeuw, Polarizable force field development and molecular dynamics study of phosphate-based glasses, J. Chem. Phys. **137**, 234502 (2012).

[34] E. Gambuzzi, A. Pedone, M. C. Menziani, F. Angeli, D. Caurant, and T. Charpentier, Probing silicon and aluminium chemical environments in silicate and aluminosilicate glasses by solid state NMR spectroscopy and accurate first-principles calculations, Geochim. Cosmochim. Acta **125**, 170 (2014).

[35] G. Malavasi, A. Pedone, and M. C. Menziani, Study of the structural role of gallium and aluminum in 45S5 bioactive glasses by molecular dynamics simulations, J. Phys. Chem. B **117**, 4142 (2013).

[36] A. Pedone, X. Chen, R. G. Hill, and A. Karpukhina, Molecular dynamics investigation of halide-containing phospho-silicate bioactive glasses, J. Phys. Chem. B **122**, 2940 (2018).

[37] P. C. M. Fossati, T. A. Mellan, N. Kuganathan, and W. E. Lee, Atomistic modeling approach to the thermodynamics of sodium silicate glasses, J. Am. Ceram. Soc. **104**, 1331 (2021).

[38] M. Fortino, A. Berselli, N. Stone-Weiss, L. Deng, A. Goel, J. Du, and A. Pedone, Assessment of interatomic parameters for the reproduction of borosilicate glass structures via DFT-GIPAW calculations, J. Am. Ceram. Soc. **102**, 7225 (2019).

[39] A. Pedone, Recent advances in solid-state NMR computational spectroscopy: the case of alumino-silicate glasses, Int. J. Quantum Chem. **116**, 1520 (2016).

[40] F. Lodesani, M. C. Menziani, H. Hijiya, Y. Takato, S. Urata, and A. Pedone, Structural origins of the mixed alkali effect in alkali aluminosilicate glasses: molecular dynamics study and its assessment, Sci. Rep. **10**, 1 (2020).

[41] A. Pedone, E. Gambuzzi, and M. C. Menziani, Unambiguous description of the oxygen environment in multicomponent aluminosilicate glasses from ^{17}O solid state NMR computational spectroscopy, J. Phys. Chem. C **116**, 14599 (2012).

[42] A. Pedone, E. Gambuzzi, G. Malavasi, and M. C. Menziani, First-principles simulations of the ^{27}Al and ^{17}O solid-state NMR spectra of the $CaAl_2Si_3O_{10}$ glass, Theor. Chem. Acc. **131**, 1147 (2012).

[43] See Supplemental Material at https://link.aps.org/supplemental/10.1103/PhysRevMaterials.5.045602 for the description of the SHIK and CSM FFs and their parameters; atomic compositions and simulation box dimensions of the systems investigated; description of glass generation and the properties calculations; density trends of investigated glass families, Young's modulus of binary silicate, and aluminosilicate glasses, total distribution functions of v-silica; P and Al coordination numbers; Si-O-Si and Si-O-P BADs of binary silicate and phoshosilicate glasses; Q^n distribution of Si in 45S5 Bioglass; VDOS of v-silica, which include Refs. [13,15,18,37–40,42,46,48,50,51,75,99–120].

[44] L. Pauling, The nature of the chemical bond. Application of results obtained from the quantum mechanics and from a theory of paramagnetic susceptibility to the structure of molecules, J. Am. Chem. Soc. **53**, 1367 (1931).

[45] F. Noritake and K. Kawamura, The nature of Si-O-Si bonding via molecular orbital calculations, J. Comput. Chem. Jpn. **14**, 124 (2015).

[46] J. D. Gale and A. L. Rohl, The general utility lattice program (GULP), Mol. Simul. **29**, 291 (2003).

[47] J. P. Perdew, A. Ruzsinszky, G. I. Csonka, O. A. Vydrov, G. E. Scuseria, L. A. Constantin, X. Zhou, and K. Burke, Restoring the Density-Gradient Expansion for Exchange in Solids and Surfaces, Phys. Rev. Lett. **102**, 039902 (2009).

[48] M. D. Segall, P. J. D. Lindan, M. J. Probert, C. J. Pickard, P. J. Hasnip, S. J. Clark, and M. C. Payne, First-Principles simulation: ideas, illustrations and the CASTEP code, J. Phys. Condens. Matter **14**, 2717 (2002).

[49] G. Ori, M. Montorsi, A. Pedone, and C. Siligardi, Insight into the structure of vanadium containing glasses: a molecular dynamics study, J. Non-Cryst. Solids **357**, 2571 (2011).

[50] D. Presti, A. Pedone, D. Licari, and V. Barone, A modular implementation for the simulation of 1D and 2D solid-state NMR spectra of quadrupolar nuclei in the virtual multifrequency spectrometer-draw graphical interface, J. Chem. Theory Comput. **13**, 2215 (2017).

[51] T. Charpentier, M. C. Menziani, and A. Pedone, Computational simulations of solid state NMR spectra: a new era in structure determination of oxide glasses, RSC Adv. **3**, 10550 (2013).

[52] Y. Xiang, J. Du, M. M. Smedskjaer, and J. C. Mauro, Structure and properties of sodium aluminosilicate glasses from molecular dynamics simulations, J. Chem. Phys. **139**, 044507 (2013).

[53] R. Hill, An alternative view of the degradation of Bioglass, J. Mater. Sci. Lett. **15**, 1122 (1996).

[54] A. J. Parsons, I. Ahmed, C. D. Rudd, G. J. Cuello, E. Pellegrini, D. Richard, and M. R. Johnson, Neutron scattering and *ab initio* molecular dynamics study of cross-linking in biomedical phosphate glasses, J. Phys. Condens. Matter **22**, 485403 (2010).

[55] A. C. Wright, Neutron and x-ray amorphography, J. Non-Cryst. Solids **106**, 1 (1988).

[56] A. C. Wright, The comparison of molecular dynamics simulations with diffraction experiments, J. Non-Cryst. Solids **159**, 264 (1993).

[57] A. K. Pant and D. W. J. Cruickshank, The crystal structure of α-$Na_2Si_2O_5$, Acta Crystallogr. B **24**, 13 (1968).

[58] J. Zhao, P. H. Gaskell, M. M. Cluckie, and A. K. Soper, A neutron diffraction, isotopic substitution study of the structure of $Li_2O \cdot 2SiO_2$ glass, J. Non-Cryst. Solids **232–234**, 721 (1998).

[59] C. Mazzara, J. Jupille, A.-M. Flank, and P. Lagarde, Stereochemical order around sodium in amorphous silica, J. Phys. Chem. B **104**, 3438 (2000).

[60] M. Benoit, S. Ispas, and M. E. Tuckerman, Structural properties of molten silicates from *ab initio* molecular-dynamics simulations: comparison between CaO-Al_2O_3-SiO_2 and SiO_2, Phys. Rev. B **64**, 224205 (2001).

[61] R. D. Shannon, Revised effective ionic radii and systematic studies of interatomic distances in halides and chalcogenides, Acta Crystallogr. A **32**, 751 (1976).

[62] T. M. Clark, P. J. Grandinetti, P. Florian, and J. F. Stebbins, Correlated structural distributions in silica glass, Phys. Rev. B **70**, 064202 (2004).

[63] T. Charpentier, P. Kroll, and F. Mauri, First-principles nuclear magnetic resonance structural analysis of vitreous silica, J. Phys. Chem. C **113**, 7917 (2009).

[64] W. J. Malfait, W. E. Halter, and R. Verel, ^{29}Si NMR spectroscopy of silica glass: T_1 relaxation and constraints on the Si-O-Si bond angle distribution, Chem. Geol. **256**, 269 (2008).

[65] K. Baral, A. Li, and W.-Y. Ching, *Ab initio* modeling of structure and properties of single and mixed alkali silicate glasses, J. Phys. Chem. A **121**, 7697 (2017).

[66] B. Hehlen, D. R. Neuville, D. Kilymis, and S. Ispas, Bimodal distribution of Si-O-Si angles in sodo-silicate glasses, J. Non-Cryst. Solids **469**, 39 (2017).

[67] P. A. Madden and M. Wilson, 'Covalent' effects in 'ionic' systems, Chem. Soc. Rev. **25**, 339 (1996).

[68] H. Yu and W. F. van Gunsteren, Accounting for polarization in molecular simulation, Comput. Phys. Commun. **172**, 69 (2005).

[69] U. Voigt, H. Lammert, H. Eckert, and A. Heuer, Cation clustering in lithium silicate glasses: quantitative description by solid-state NMR and molecular dynamics simulations, Phys. Rev. B **72**, 064207 (2005).

[70] H. Maekawa, P. Florian, D. Massiot, H. Kiyono, and M. Nakamura, Effect of alkali metal oxide on ^{17}O NMR parameters and Si-O-Si angles of alkali metal disilicate glasses, J. Phys. Chem. **100**, 5525 (1996).

[71] W. J. Malfait, W. E. Halter, Y. Morizet, B. H. Meier, and R. Verel, Structural control on bulk melt properties: single and double quantum ^{29}Si NMR spectroscopy on alkali-silicate glasses, Geochim. Cosmochim. Acta **71**, 6002 (2007).

[72] R. Mathew, B. Stevensson, A. Tilocca, and M. Edén, Toward a rational design of bioactive glasses with optimal structural features: composition-structure correlations unveiled by solid-state NMR and MD simulations, J. Phys. Chem. B **118**, 833 (2014).

[73] L. L. Hench, The story of Bioglass®, J. Mater. Sci. Mater. Med. **17**, 967 (2006).

[74] D. M. Pickup, I. Ahmed, P. Guerry, J. C. Knowles, M. E. Smith, and R. J. Newport, The structure of phosphate glass biomaterials from neutron diffraction and ^{31}P nuclear magnetic resonance data, J. Phys. Condens. Matter **19**, 415116 (2007).

[75] R. K. Brow, Review: The structure of simple phosphate glasses, J. Non-Cryst. Solids **263–264**, 1 (2000).

[76] M. Edén, The split network analysis for exploring composition-structure correlations in multi-component glasses: I. rationalizing bioactivity-composition trends of bioglasses, J. Non-Cryst. Solids **357**, 1595 (2011).

[77] T. Uchino, T. Sakka, Y. Ogata, and M. Iwasaki, Local structure of sodium aluminosilicate glass: an *ab initio* molecular orbital study, J. Phys. Chem. **97**, 9642 (1993).

[78] J. R. Allwardt, S. K. Lee, and J. F. Stebbins, Bonding preferences of non-bridging O atoms: evidence from ^{17}O MAS and 3QMAS NMR on calcium aluminate and low-silica Ca-aluminosilicate glasses, Am. Mineral. **88**, 949 (2003).

[79] W. Loewenstein, The distribution of aluminum in the tetrahedra of silicates and aluminates, Am. Mineral. **39**, 92 (1954).

[80] J. F. Stebbins, S. K. Lee, and J. V. Oglesby, Letters. Al-O-Al oxygen sites in crystalline aluminates and aluminosilicate glasses: high-resolution oxygen-17 NMR results, Am. Mineral. **84**, 983 (1999).

[81] S. K. Lee and J. F. Stebbins, Al-O-Al and Si-O-Si sites in framework aluminosilicate glasses with Si/Al = 1: quantification of framework disorder, J. Non-Cryst. Solids **270**, 260 (2000).

[82] P. Richet, Viscosity and configurational entropy of silicate melts, Geochim. Cosmochim. Acta **48**, 471 (1984).

[83] S. K. Lee and J. F. Stebbins, The degree of aluminum avoidance in aluminosilicate glasses, Am. Mineral. **84**, 937 (1999).

[84] J. F. Stebbins and S. Sen, Oxide ion speciation in potassium silicate glasses: new limits from ^{17}O NMR, J. Non-Cryst. Solids **368**, 17 (2013).

[85] H. Maekawa, T. Maekawa, K. Kawamura, and T. Yokokawa, The structural groups of alkali silicate glasses determined from ^{29}Si MAS-NMR, J. Non-Cryst. Solids **127**, 53 (1991).

[86] A. Pedone, T. Charpentier, G. Malavasi, and M. C. Menziani, New Insights into the atomic structure of 45S5 Bioglass by means of solid-state NMR spectroscopy and accurate first-principles simulations, Chem. Mater. **22**, 5644 (2010).

[87] R. Witter, P. Hartmann, J. Vogel, and C. Jäger, Measurements of chain length distributions in calcium phosphate glasses using 2D ^{31}P double quantum NMR, Solid State Nucl. Magn. Reson. **13**, 189 (1998).

[88] A. Soleilhavoup, J.-M. Delaye, F. Angeli, D. Caurant, and T. Charpentier, Contribution of first-principles calculations to multinuclear NMR analysis of borosilicate glasses, Magn. Reson. Chem. **48**, S159 (2010).

[89] N. P. Bansal and R. H. Doremus, Elastic properties, in *Handbook of Glass Properties*, edited by N. P. Bansal and R. H. Doremus (Academic Press, San Diego, 1986), Chap. 10, pp. 306–336.

[90] A. Pedone, G. Malavasi, A. N. Cormack, U. Segre, and M. C. Menziani, Insight into elastic properties of binary alkali silicate glasses; prediction and interpretation through atomistic simulation techniques, Chem. Mater. **19**, 3144 (2007).

[91] J. O. Isard, The mixed alkali effect in glass, J. Non-Cryst. Solids **1**, 235 (1969).

[92] J. E. Tsuchida, F. A. Ferri, P. S. Pizani, A. C. M. Rodrigues, S. Kundu, J. F. Schneider, and E. D. Zanotto, Ionic conductivity and mixed-ion effect in mixed alkali metaphosphate glasses, Phys. Chem. Chem. Phys. **19**, 6594 (2017).

[93] R. K. Sato, R. J. Kirkpatrick, and R. K. Brow, Structure of Li,Na metaphosphate glasses by ^{31}P and ^{23}Na MAS-NMR correlated with the mixed alkali effect, J. Non-Cryst. Solids **143**, 257 (1992).

[94] M. D. Ingram and A. H. Jean Robertson, Ion transport in glassy electrolytes, Solid State Ion. **94**, 49 (1997).

[95] M. D. Ingram, Towards a theory of ion transport in glass, Phys. Stat. Mech. Its Appl. **266**, 390 (1999).

[96] M. D. Ingram, C. T. Moynihan, and A. V. Lesikar, Ionic conductivity and the weak electrolyte theory of glass, J. Non-Cryst. Solids **38–39**, 371 (1980).

[97] S. R. Elliott, Frequency-dependent conductivity in ionic glasses: a possible model, Solid State Ion. **27**, 131 (1988).

[98] A. Pedone, G. Malavasi, M. C. Menziani, U. Segre, F. Musso, M. Corno, B. Civalleri, and P. Ugliengo, FFSiOH: A new force field for silica polymorphs and their hydroxylated surfaces based on periodic B3LYP calculations, Chem. Mater. **20**, 2522 (2008).

[99] D. Wolf, P. Keblinski, S. R. Phillpot, and J. Eggebrecht, Exact method for the simulation of Coulombic systems by spherically truncated, pairwise r^{-1} summation, J. Chem. Phys. **110**, 8254 (1999).

[100] S. Sundararaman, L. Huang, S. Ispas, and W. Kob, New optimization scheme to obtain interaction potentials for oxide glasses, J. Chem. Phys. **148**, 194504 (2018).

[101] J. D. Gale, Empirical potential derivation for ionic materials, Philos. Mag. Part B **73**, 3 (1996).

[102] WWW-MINCRYST—Crystallographic Database for Minerals, http://database.iem.ac.ru/mincryst/.

[103] W. Smith and T. R. Forester, DL_POLY_2.0: a general-purpose parallel molecular dynamics simulation package, J. Mol. Graph. **14**, 136 (1996).

[104] M. P. Allen, M. P. Allen, D. J. Tildesley, and D. J. Tildesley, *Computer Simulation of Liquids*, (Clarendon Press, Oxford, 1989).

[105] L. Deng and J. Du, Effects of system size and cooling rate on the structure and properties of sodium borosilicate glasses from molecular dynamics simulations, J. Chem. Phys. **148**, 024504 (2018).

[106] X. Li, W. Song, K. Yang, N. M. A. Krishnan, B. Wang, M. M. Smedskjaer, J. C. Mauro, G. Sant, M. Balonis, and M. Bauchy, Cooling rate effects in sodium silicate glasses: bridging the gap between molecular dynamics simulations and experiments, J. Chem. Phys. **147**, 074501 (2017).

[107] M. Pota, A. Pedone, G. Malavasi, C. Durante, M. Cocchi, and M. C. Menziani, Molecular dynamics simulations of sodium silicate glasses: optimization and limits of the computational procedure, Comput. Mater. Sci. **47**, 739 (2010).

[108] A. Tilocca, Cooling rate and size effects on the medium-range structure of multicomponent oxide glasses simulated by molecular dynamics, J. Chem. Phys. **139**, 114501 (2013).

[109] K. Vollmayr, W. Kob, and K. Binder, Cooling-rate effects in amorphous silica: a computer-simulation study, Phys. Rev. B **54**, 15808 (1996).

[110] A. Pedone, G. Malavasi, M. C. Menziani, U. Segre, and A. N. Cormack, Molecular dynamics studies of stress-strain behavior of silica glass under a tensile load, Chem. Mater. **20**, 4356 (2008).

[111] P. K. Gupta and C. R. Kurkjian, Intrinsic failure and non-linear elastic behavior of glasses, J. Non-Cryst. Solids **351**, 2324 (2005).

[112] C. Müller, E. Zienicke, S. Adams, J. Habasaki, and P. Maass, Comparison of ion sites and diffusion paths in glasses obtained by molecular dynamics simulations and bond valence analysis, Phys. Rev. B **75**, 014203 (2007).

[113] C. J. Pickard and F. Mauri, All-electron magnetic response with pseudopotentials: NMR chemical shifts, Phys. Rev. B **63**, 245101 (2001).

[114] P. E. Blöchl, Projector augmented-wave method, Phys. Rev. B **50**, 17953 (1994).

[115] J. P. Perdew, K. Burke, and M. Ernzerhof, Generalized Gradient Approximation Made Simple, Phys. Rev. Lett. **77**, 3865 (1996).

[116] Y. Xiang and J. Du, Effect of strontium substitution on the structure of 45S5 bioglasses, Chem. Mater. **23**, 2703 (2011).

[117] T. Charpentier, K. Okhotnikov, A. N. Novikov, L. Hennet, H. E. Fischer, D. R. Neuville, and P. Florian, Structure of strontium aluminosilicate glasses from molecular dynamics simulation, neutron diffraction, and nuclear magnetic resonance studies, J. Phys. Chem. B **122**, 9567 (2018).

[118] A. Hiramatsu, M. Arai, H. Shibazaki, M. Tsunekawa, T. Otomo, A. C. Hannon, S. M. Bennington, N. Kitamura, and A. Onodera, Investigation on permanently densified vitreous silica by means of neutron scattering, Phys. B Condens. Matter **219–220**, 287 (1996).

[119] U. Buchenau, M. Prager, N. Nücker, A. J. Dianoux, N. Ahmad, and W. A. Phillips, Low-frequency modes in vitreous silica, Phys. Rev. B **34**, 5665 (1986).

[120] M. Handke and W. Mozgawa, Model quasi-molecule Si_2O as an approach in the IR spectra description glassy and crystalline framework silicates, J. Mol. Struct. **348**, 341 (1995).